Theses and Dissertations

5-2015

Mirror Buckling Transitions in Freestanding Graphene Membranes induced through Scanning Tunneling Microscopy

James Kevin Schoelz
University of Arkansas, Fayetteville

Follow this and additional works at: http://scholarworks.uark.edu/etd

 Part of the Biophysics Commons, Condensed Matter Physics Commons, and the Quantum Physics Commons

Mirror Buckling Transitions in Freestanding Graphene Membranes Induced through Scanning Tunneling Microscopy

Mirror Buckling Transitions in Freestanding Graphene Membranes Induced through
Scanning Tunneling Microscopy

A dissertation submitted in partial fulfillment
of the requirements for the degree of
Doctor of Philosophy in Physics

By

James K. Schoelz
Truman State University
Bachelor of Science in Physics 2010
University of Arkansas
Master of Science in Physics 2014

May 2015
University of Arkansas

This dissertation is approved for recommendation to the Graduate Council
Dissertation Director:

_____

Dr. Paul M. Thibado
Dissertation Director

_____   _____

Dr. William Oliver   Dr. William Harter
 Committee Member   Committee Member

_____   _____

Dr. Reeta Vyas   Dr. Jingyi Chen
Committee Member   Committee Member

Abstract

Graphene has the ability to provide for a technological revolution. First isolated and characterized in 2004, this material shows promise in the field of flexible electronics. The electronic properties of graphene can be tuned by controlling the shape of the membrane. Of particular interest in this endeavor are the thermal ripples in graphene membranes. Years of theoretical work by such luminaries as Lev Landau, Rudolf Peierls, David Mermin and Herbert Wagner have established that 2D crystals should not be thermodynamically stable. Experimental research on thin films has supported this finding. Yet graphene exists, and freestanding graphene films have been grown on large scales. It turns out that coupling between the bending and stretching phonons can stabilize the graphene in a flat, albeit rippled phase. These ripples have attracted much attention, and recent work has shown how to arrange these ripples in a variety of configurations.

In this thesis, I will present work done using a scanning tunneling microscope (STM) to interact with freestanding graphene membranes. First I will present STM images of freestanding graphene and show how these images show signs of distortion under the electrostatic influence of the STM tip. This electrostatic attraction between the STM tip and the graphene sample can be used to pull on the graphene sample. At the same time, by employing Joule heating in order to heat graphene using the tunneling current, and exploiting the negative coefficient of thermal expansion, a repulsive thermal load can be generated.

By repeatedly pulling on the graphene using the electrostatic potential, while sequentially increasing the setpoint current we can generate a thermal mirror buckling event. Slowly heating the graphene using the tunneling current, prepares a small convex region of graphene under the tip. By increasing thermal stress, as well as pulling using the out of plane electrostatic force, the graphene suddenly and irreversibly switches the sign of its curvature. This event is discovered using STM measurements and supplemented by molecular dynamics simulations.

Finally, I will show how to characterize this transition using the famed Ising model. The ripples are modeled as individual Ising spins, which at low temperature exhibit antiferromagnetic coupling. By heating the graphene membrane, the strain increases, changing the antiferromagnetic coupling to ferromagnetic coupling, which characterizes the irreversible transition from a soft, flexible state to a rigid configuration.

Acknowledgments

I would like to start out by thanking my doctoral advisor, Dr. Paul Thibado. I have enjoyed my time working in his lab, and have learned a lot from him. During my time here, I have had the opportunity to work along many wonderful individuals such as Peng Xu, Steven Barber, Matt Ackerman, Dejun Qi, Cameron Cook, Gobind Basnet, Pijush Ghosh and Josh Thompson. In addition, I would like to thank a few of our numerous collaborators, Dr. Pradeep Kumar at the University of Arkansas, Dr. Vincent Meunier at Renssalaer Polytechnic Institute, Dr. Lifeng Dong at Missouri State University, Dr. Mehdi Neek-Amal and Dr. Francois Peeters at Universiteit Antwerpen.

I also want to thank my committee members for taking the time to help and review my progress, including Dr. Lin Oliver, Dr. Bill Harter, Dr. Reeta Vyas of the physics department, and Dr. Jingyi Chen of the chemistry department.

My parents have always encouraged me to pursue my education, and from an early age, instilled in me a love of learning. I am eternally grateful for their support. Last, but certainly not least, I want to thank my wife, Santoshi. She has been so supportive throughout my graduate career. I don't know how I would have been able to complete this without her.

Contents

List of Figures

List of Tables

Chapter 1

Introduction

Graphene, a 2D allotrope of carbon, was first isolated and characterized in 2004 in a series of papers by Novoselov *et al.* at the University of Manchester[1–3]. Due to its many amazing properties, the study of graphene has become very popular in recent years[4, 5].

Much of the initial excitement around graphene could be related to its technological promise. The charge carriers in graphene show very high mobilities[6–8], and have even displayed ballistic transport[9, 10]. It also has a record breaking thermal conductivity[11]. Graphene has potential in the fields of heterojunction solar cells[12] as well as fuel cells[13, 14]. Many groups have managed to produce graphene actuators[15] and resonators[16, 17]. Measurements of the breaking strength of graphene membranes have revealed it to among the strongest materials in the world[18]

In addition to its technological promise, graphene also provides a material in which researchers can conduct benchtop quantum electrodynamics experiments[4]. Graphene has a linear bandstructure, as first predicted by P.R. Wallace in 1947[19]. Thus, electrons in graphene behave as massless, chiral Dirac fermions[20, 21]. An implication of this is that graphene should have an anomalous quantum hall effect. This behavior was confirmed experimentally in 2005 by two teams of researchers[2, 22]. In addition, researchers have shown that the opacity of these atomically thin graphene films is determined by the fine structure constant[23].

In this chapter we will briefly review and derive some of the basic properties of graphene membranes.
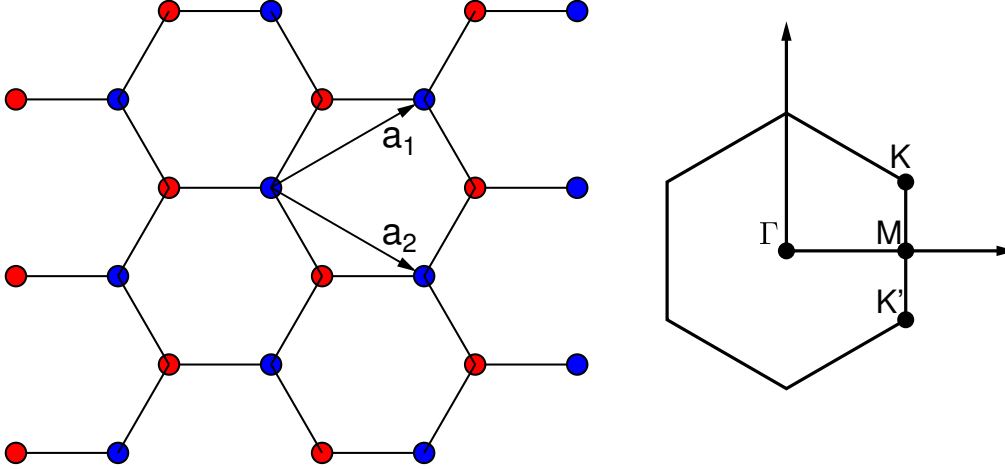
Figure 1.1: (left) Schematic showing a hexagonal lattice. The two Bravais sublattices are shown in blue and yellow. One possible set of lattice vectors is shown in the figure and labeled as a_1 and a_2 (right) Illustration of Brillouin zone for graphene. High symmetry points are labeled.

1.1 Graphene: structure

Graphene consists of a single layer of carbon atoms arranged in a hexagonal lattice, as shown in Fig. 1.1. The carbon atoms each contribute four valence electrons. Three of these electrons are in sp_2 hybridized states that result in the σ bonds binding the carbon atoms together. These σ bands are responsible for the remarkable in-plane strength of graphene. The fourth electron is in the $2p_z$ orbital, which extends above and below the atomic plane. These electrons are delocalized, and form the π band, which is responsible for most of graphene's remarkable electronic properties.

Graphene has two carbon atoms in each unit cell, with each atom usually denoted as belonging to the A and B Bravais sublattices of graphene. We can characterize this structure using a particularly convenient choice of lattice vectors

$$\boldsymbol{a} = \left(\pm \frac{3a}{2}, \frac{a\sqrt{3}}{2} \right) \tag{1.1}$$

where $a = 1.42$ nm is the carbon-carbon bond distance. With this convention, we can write

2

down the nearest neighbor vectors as

$$\boldsymbol{\delta}_1 = \frac{a}{2}\left(1, \sqrt{3}\right) \tag{1.2a}$$

$$\boldsymbol{\delta}_2 = \frac{a}{2}\left(1, -\sqrt{3}\right) \tag{1.2b}$$

$$\boldsymbol{\delta}_3 = -a\left(1, 0\right) \tag{1.2c}$$

From the lattice vectors given above, we can define a set of reciprocal lattice vectors using the relation $\boldsymbol{a}_i \cdot \boldsymbol{b}_j = 2\pi\delta_{ij}$. The reciprocal lattice vectors are then given by

$$\boldsymbol{b} = \left(\pm\frac{4\pi}{3a}, \frac{4\pi}{a\sqrt{3}}\right) \tag{1.3}$$

The Brillouin zone, calculated from the reciprocal lattice vectors given above, is shown in Fig. 1.1. The corners of the Brillouin zone are labeled as $\boldsymbol{K}$ and $\boldsymbol{K}'$, and have coordinates

$$\boldsymbol{K} = \frac{2\pi}{3a}\left(1, \frac{\sqrt{3}}{3}\right) \tag{1.4a}$$

$$\boldsymbol{K}' = \frac{2\pi}{3a}\left(1, -\frac{\sqrt{3}}{3}\right) \tag{1.4b}$$

1.1.1   Tight binding model

The band structure of graphene was first calculated by P.R. Wallace in 1947[19] using the tight binding model. Since graphene was not considered a realistic possibility, his calculation of the graphene bandstructure was obtained as an intermediate step towards calculating the bandstructure of a graphite crystal. In fact, a lot of theoretical work went into evaluating the theoretical bandstructure of graphene before 2004, as this was an important step towards evaluating the properties of such carbon allotropes as carbon nanotubes and buckyballs. Semenoff looked at the bandstructure of graphene in a 1984 paper that evaluated this system

in order to see quantum field theory results in reduced dimensions[20].

For graphene, we can define the creation operators, $\hat{a}$ and $\hat{b}$, where $\hat{a}$ creates an electron on the A sublattice, and $\hat{b}$ creates an electron on the B sublattice. Their Hermitian conjugates represent the annihilation field operators. Then, the tight binding Hamiltonian for graphene is given by

$$\mathcal{H} = -t \sum_{<i,j>} \left(\hat{a}_i \hat{b}_j^\dagger + H.c. \right) \tag{1.5}$$

and choosing units such that $\hbar = 1$. The hopping parameter t, is an energy characterizing the liklihood of the electron to "hop" from one atom to one of the nearest neighbor atoms. In order to calculate the bandstructure, we can rewrite the creation operators in reciprocal space using a Fourier transform

$$\hat{a}_i = \frac{1}{\sqrt{N}} \sum_{\vec{k}} a(\boldsymbol{k}) e^{i\boldsymbol{k} \cdot \boldsymbol{R}_i} \tag{1.6}$$

Then, in reciprocal space, the tight binding Hamiltonian becomes

$$H_{\boldsymbol{k}} = \begin{pmatrix} 0 & \varepsilon(\boldsymbol{k}) \\ \varepsilon^*(\boldsymbol{k}) & 0 \end{pmatrix} \tag{1.7}$$

where $\varepsilon(\boldsymbol{k}) = -t \left(e^{i\boldsymbol{k} \cdot \boldsymbol{\delta}_1} + e^{i\boldsymbol{k} \cdot \boldsymbol{\delta}_2} + e^{i\boldsymbol{k} \cdot \boldsymbol{\delta}_3} \right)$. The bandstructure can be found by evaluating the eigenvalues of the Hamiltonian.

$$E_\pm = \pm|\varepsilon(\boldsymbol{k})| \pm t \sqrt{3 + 2\cos\left(k_y a \sqrt{3}\right) + 4\cos\left(k_y a \frac{\sqrt{3}}{2}\right) \cos\left(k_x a \frac{3}{2}\right)} \tag{1.8}$$

The hopping parameter, t, can be found by comparing the above expression to first principle calculations near high symmetry points. For graphene, t is estimated to be 2.8 eV. Notice that in the above equation, the conduction and valence bands are symmetric. This is only

true so long as we ignore the contributions from next nearest neighbor hopping.

Graphene is a zero bandgap material. This is a consequence of the inversion symmetry of the A and B sublattices. Breaking this inversion symmetry can cause the opening of a small bandgap which is of great technological interest.

The conduction and valence bands touch at two locations in the Brillouin zone denoted by the K and K' points. We can look at the bandstructure near these points by defining $\boldsymbol{q} = \boldsymbol{k} - \boldsymbol{K}$, and looking at the Taylor expansion of the function $\varepsilon(\boldsymbol{q})$. This gives

$$\varepsilon(\boldsymbol{q}) \approx -\frac{3ta}{2}(\exp^{i2\pi/3} q_x + \exp^{-i2\pi/3} q_y) \tag{1.9}$$

Using this simplification, we can rewrite Eq 1.7 as

$$H_{\boldsymbol{q}} = -v_F \boldsymbol{\sigma} \cdot \boldsymbol{q} \tag{1.10}$$

where the elements of $\boldsymbol{\sigma}$ are the Pauli matrices, and $v_F = \frac{3ta}{2}$ is the Fermi velocity of graphene. This is the Dirac equation. Experimental results estimate the Fermi velocity in graphene to be $\sim 10^6$ m/s.

This shows that low energy excitations in graphene act as massless Dirac fermions, as confirmed by experiment[2, 22]. In this language, the A and B sublattices act as psuedospins for these Dirac Fermions. Conservation of the pseudospin is thought to explain ballistic transport on the order of microns in carbon nanotubes[21]. Second, we are currently only looking at the excitations around the K point. A similar expansion, carried out near the K' point shows that there are acturally two sets of Dirac fermions in graphene[5, 20]. Thus, in graphene, electrons can be characterized by their spin, pseudospin (to which sublattice the electron belongs) as well as the valley (excitations near either the K or K' points).

1.1.2 Pseudomagnetic fields in graphene

These properties are modified when a strain field is applied to system. Bending graphene changes the relative orientation of the p_z orbitals. This, along with stretching the carbon-carbon bond distance results in local changes to the hopping energy, t. The modification of t, in the presence of a smoothly varying strain field $u_{ij}(x, y)$ gives rise to a vector potential

$$\boldsymbol{A} = \frac{\beta}{a} \left(u_{xx} - u_{yy}, 2u_{xy} \right) \tag{1.11}$$

So electrons in a strained graphene membrane behave as if they were under the influence of a magnetic field. It is important to note however, that the Hamiltonian of the system displays time reversal symmetry. A true magnetic field would break this time reversal symmetry, however it is not broken by a strain field. Instead, recall that there are two K points in the Brillouin zone. The strain field shifts the two K points in opposite directions, preserving time reversal symmetry. This implies that the gauge vector potential does not give rise to a real magnetic field, but rather a pseudo-magnetic field[5, 24].

Work by Guinea *et al.* analyzed the form of the pseudo-magnetic field in order to ascertain a method to generate a large uniform field. They found using Equation 1.11 that an isotropic strain would not generate a gauge vector field. Instead by using a strain with trigonal symmetry it would be possible to generate a large, uniform pseudo-magnetic field[24]. This was confirmed by Levy *et al.* who discovered pseudomagnetic fields of up to 300 T in graphene nanobubbles[25].

1.2 Fabrication of graphene membranes

1.2.1 Manual exfoliation

There are many techniques used to fabricate graphene membranes. By far, the most well known technique is manual exfoliation, which was originally advertised as the scotch tape method[1, 2]. This technique gives rise to the highest quality graphene crystals, however

there are a few drawbacks. The first is that the size of the crystals produced by this method are typically on the order of a few microns. The second is that this is a very labor intensive method. In fact, graphene crystals produced by manual exfoliation are among the most expensive materials in the world.

Nonetheless, the method itself is quite simple. Highly oriented pyrolytic graphite (HOPG) consists of graphene layered in a stacked form. The graphene layers are loosely bound to each other through Van der Waal's attraction. In the manual exfoliation technique, the researcher applies some tape to the top layer of HOPG, and then pulls the tape off. This tape will have multilayer graphene. By iterating this process, it is possible to generate single layer graphene. Typically, the thickness of the crystals are measured using atomic force microscopy (AFM) to ensure that the final crystal is indeed single layer graphene.

1.2.2 Epitaxial growth

A more technologically promising route involves the thermal decomposition of SiC crystals[26]. As the SiC crystal is heated, the Si atoms leave the surface, and the remaining carbon atoms rearrange themselves in order to form a graphene layer. The graphitization of SiC has been known for over 100 years. This technique has several advantages from a technological point of view. First the graphene crystals are much larger than those produced by manual exfoliation. Second, it is compatible with existing wafer technology. In addition, SiC is a good substrate for graphene as well. It is a large bandgap semiconductor, so current flowing through graphene will not leak into the bulk SiC crystal.

There are still a few problems. SiC is a polar material, meaning that is has a Si face, as well as a C face. Growth on the Si face is slower and more coherent allowing for the production of larger graphene sheets[27]. However, the first layer of carbon atoms to form is not graphene, but rather a buffer layer that is still coupled electronically to the bulk SiC crystal. Subsequent graphene layers grown on top of this buffer layer show degraded performance due to the presence of this carbon buffer layer[28].

Growth on the C face does not give a carbon buffer layer, but the graphene obtained on this side grows faster, making it difficult to limit growth to single layer graphene, and shows a large degree of rotational disorder. Exploring growth on miscuts of the SiC faces is a promising area of research for maximizing the potential of epitaxially grown graphene, while minimizing the problems. [10, 27, 29–31].

1.2.3 Chemical vapor deposition

Much attention has been given to using chemical vapor deposition (CVD) to grow large graphene sheets. In a typical CVD process a metal foil is placed in a vacuum chamber. Methane gas (CH_4) flows over the foil. The metal atoms catalyze a reaction in which carbon atoms are deposited onto the foil forming monolayer graphene[32]. A number of metal foils can be used including copper and nickel.

Using this method, single crystal graphene membranes as large as 5 mm have been grown[32]. However, Bae *et al.* have developed a technique which allows roll to roll production of 30 in polycrystalline graphene films[33].

1.3 Graphene on a substrate

Graphene has many amazing properties, however, most applications have graphene supported by some sort of substrate. This results in a few issues. Zhang *et al.* looked at manually exfoliated graphene on a SiO_2 substrate using scanning tunneling microscopy (STM). By looking at the spatially resolved differential tunneling conductance (dI/dV) they were able to map the local density of states of their graphene sample. A large degree of charge puddling was observed, which would degrade the transport properties of the graphene sample. This charge puddling was attributed not to any intrinsic property of the graphene itself, but rather the supporting substrate[34].

Chemical vapor deposition of graphene on copper foil is one of the most promising methods for the large scale fabrication of graphene sheets. However often it needs to be transferred

to other substrates. This involves coating the graphene using poly(methyl methacrylate) (PMMA), and then etching away the copper. The graphene is then transferred to the substrate of choice. The PMMA is removed by annealing the sample. A 2011 study by Pirkle and coworkers found that this method leaves some residues on the graphene which negatively affect performance[35].

1.4 Flexural phonon modes

One of the more remarkable properties of graphene is its very existence. Years of theoretical work culminating in the Mermin-Wagner theorem had established that purely 2D crystals should be thermodynamically unstable[36, 37]. Experiments looking at the melting temperatures of thin films seemed to support this view[38, 39]. However, Fasolino *et al.* clarified that in fact, coupling between the bending and stretching modes would suppress these thermal fluctuations, and leave the graphene membrane in a rippled state[40]. So the graphene membrane resembles a network of hemispheres alternately curved up or down. These out of plane fluctuations are critical to the existence of graphene[41–43].

Since the discovery of graphene, much work has gone into understanding these flexural phonon modes. They are important in explaining graphene's negative coefficient of thermal expansion[44]. As the graphene membrane is heated, the out of plane fluctuations increase, causing the graphene membrane to contract. In additions, the flexural phonon modes are responsible for the bulk of the thermal transport[45].

Meyer *et al.* made the first experimental observation of static ripples in a suspended graphene membrane using transmission electron microscopy[46]. Since then, several scanning tunneling microscope groups have managed to observe static ripple configurations[47–49]. Recent work by Xu *et al.* has even shown how to use a scanning tunneling microscope to track the ripple dynamics[50].

1.5 Summary

In this thesis we will explore the stability of 2D graphene membranes using scanning tunneling microscopy. In the next chapter I will introduce the basic concepts behind scanning tunneling microscopy, as well as how to reliably manufacture and evaluate STM tips[51]. Next I will explore what happens when STM is used to characterize a freestanding graphene membrane[52]. Specifically, we will look at the forces between the STM tip and the freestanding graphene membrane. Next we will show how to exploit these forces, in order to drive a buckling transition in graphene[53]. In the final chapter, we will show that this buckling transition can be successfully modeled using the spin-half Ising magnet[54].

Chapter 2

Scanning Tunneling Microscopy

The invention of the electron microscope at the turn of the 20th century marked a breakthrough in atomic scale physics. By showing it was possible to image samples with electrons, rather than light, researchers greatly improved the potential for imaging small features. The field emission microscope (FEM) took this a step further and for the first time allowed the imaging of individual atoms[55]. However, as the FEM required the sample to be in the form of a sharp tip, the materials that could be imaged were limited. The invention of the scanning tunneling microscope (STM) in 1981, by Gerd Binning and Heinreich Rohrer, greatly expanded the field and for the first time allowed atomic resolution imaging of flat metal and semiconductor surfaces[56–58].

The scanning tunneling microscope works by bringing a sharp metal probe to within a small distance (~ 5 Å) from a grounded sample. A potential difference is then applied to the tip-sample system, which facilitates electron tunneling from the metal tip into the sample. The extreme sensitivity of this tunneling current to the separation between the sample means that this technique is very sensitive to changes in the local density of states (LDOS), and allows the resolution of single atoms on the surface of the sample.

Using the STM, researchers were able to resolve the surface reconstructions of several technologically important surfaces. Binnig and Rohrer were able to resolve the 7×7 reconstruction of the Si(111) surface[58]. Since then, much work has been done in order to resolve the various surface reconstructions of Si [59] and GaAs[60, 61].

STM is a powerful technique, however, and it is not just limited to the imaging of surfaces.

By imaging a surface during the growth process, it is possible to obtain information about dynamics of adatoms as they move around on the surface.[62, 63] This process was first carried out by Y.W. Mo and coworkers who imaged islands on the Si(001) surface. By comparing successive STM images, it was possible to measure the growth of these islands over time and extract the diffusion coefficients of the Si adatoms.[62]. Work by Swartzentruber, improved on this by actually finding a diffusing adatom, and following its motion with the STM tip.[64]. This technique allowed the research to measure the time trajectory over long periods of time in order to more directly determine the diffusion coefficients. He acquired data over a range of tip bias conditions, and showed that at low bias, they could use the STM to passively monitor the position of the diffusing adatom.

Since the early days of STM, it has been known that the forces exerted by the tip on the sample could be utilized to build nanostructures on surfaces at an atomic scale. In a series of papers published in the early 90s, Eigler and coworkers used the STM tip to create a series of nanostructures, including arranging atoms to show the IBM logo, as well as create a standing wave patterns [65–68]. In this method, a voltage pulse could be used to pick up an adatom with the STM tip, and then deposit it at the location specified by the researcher. The tunneling current can also be used to manipulate the material at an atomic scale. By increasing the tunneling current, Stauffer *et al.* were able to locally melt nanostructures located on the surface of various metals.[69]

In this chapter we will discuss the STM measurement. We will start by reviewing some basic tunneling theory, and then using this to discuss some basic STM measurements. We will conclude by discussing the specifics of our STM system as well as our method for preparing ultrasharp STM probes.

2.1 Theory of Tunneling

2.1.1 Elastic tunneling through a rectangular barrier

Key to the success of the STM is the extreme sensitivity of the tunneling current to changes in the tip-sample distance. We can model this effect by looking at the tip-sample system as tunneling through a rectangular barrier as seen in Fig. 2.1 [70, 71]. In this case, we can write down solutions for the Schrodinger equation for a barrier of height V, and width a as

$$\psi_I = Ae^{ikx} + Be^{-ikx} \tag{2.1}$$

$$\psi_{II} = Ce^{\kappa x} + De^{-\kappa x} \tag{2.2}$$

$$\psi_{III} = Fe^{ikx} \tag{2.3}$$

where $k = \sqrt{2mE/\hbar^2}$ is the wavevector of the electron outside of the barrier, and $\kappa = \sqrt{2m(V-E)/\hbar^2}$ is the decay constant of the wavefunction inside the barrier.

By applying the boundary conditions, we can solve for the integration constants (A, B, C, D, and F), and write down the transmission coefficient,

$$T = \left[1 + \frac{\sinh^2(\kappa a)}{4\frac{E}{V}\sqrt{1 - \frac{E}{V}}} \right]^{-1} \tag{2.4}$$

For thick, impenetrable barriers, (i.e.$\kappa a \gg 1$), this simplifies to

$$T \approx 16 \left(\frac{E}{V}\sqrt{1 - \frac{E}{V}} \right) e^{-2\kappa a} \tag{2.5}$$

From this we get that the tunneling current shows an exponential dependence upon the barrier width

$$I \propto e^{-2\kappa a} \tag{2.6}$$

13
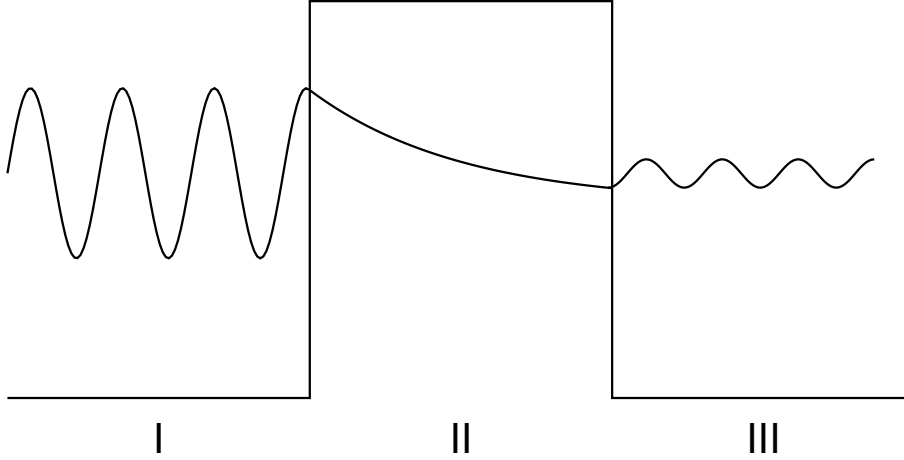
Figure 2.1: Schematic showing the tunneling of an electron wavefunction through a rectangular barrier of height V.

This exponential dependence on the barrier width means that the tunneling current is very sensitive to changes in the local density of states. For example, moving the tip inwards by 1 Å results in an order of magnitude increase in the tunneling current.

2.1.2 Time-dependent perturbation theory

An additional approach to calculate the tunneling current is using time dependent perturbation theory. In this methodology, the current tunneling from a given tip state into the sample can be calculated using Fermi's golden rule. However, in order to do this, we need to calculate the transition matrix element. The transition matrix element for tunneling from one electrode through a vacuum barrier to another electrode was first calculated by Bardeen in 1961[72] and is given by

$$M_{TS} = \frac{\hbar^2}{2m} \int \psi_T^* \nabla \psi_S - \psi_T^* \nabla \psi_S d\tau \tag{2.7}$$

where ψ_T is the wavefunction of the tip state, and ψ_S is the wavefuntion of the sample state. The full tunneling current, given by Tersoff and Hamann[73] is then given by

14
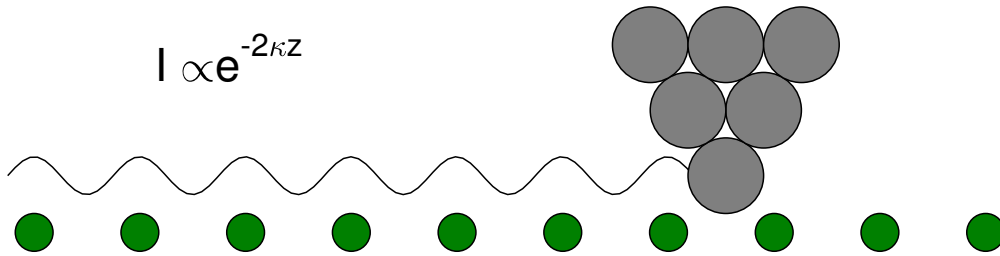
Figure 2.2: Cartoon showing the movement of an STM tip as it scans over a surface while maintaining a constant tunneling current

$$I = \frac{2\pi e}{\hbar} \int f(E_T) \left[1 - f(E_S + eV) \right] \rho_S(E_S)\rho_T(E_T)|M_{TS}|^2 \delta(E_T - E_S) \qquad (2.8)$$

2.2 STM Measurements

2.2.1 STM imaging

In an STM imaging experiment, the STM can be operated in one of two modes: constant current or constant height. In the constant current experiment, a set point current is chosen, and the tunneling current is monitored by a feedback circuit. Then, the height of the tip is adjusted by piezoelectric actuators in order to maintain the tunneling current within a given tolerance of the set point current. The tip is raster scanned across the surface, and the height of the tip is revealed as a function of the position. Tersoff and Hamann showed that the images generated by this method could be interpreted as a map of the local density of states[73].

In the constant height experiment, an initial height of the tip is chosen. The tip is raster scanned across the surface with the feedback electronics off, and the changes in the tunneling current are recorded as a function of position. The resulting image gives a map of the local density of states of the sample.

The precise control of piezoelectric actuators means that either method is capable of

generating atomic resolution images of the sample surface[70]. For this dissertation, all STM images will be taken using the constant current mode.

2.2.2 Constant height $I(V)$ spectroscopy

A common STM measurement involves holding the STM tip at a single location on the sample, sweeping through a range of tip bias values, and recording the change in the tunneling current. This measurement is commonly referred to as $I(V)$ spectroscopy. The normalized tunneling conductance has shown to be propotional to the density of states in the sample[59]

$$\frac{V}{I}\frac{dI}{dV} \propto \rho_S \tag{2.9}$$

2.2.3 Constant current $z(V)$ spectroscopy

A very similar measurement can be performed measuring the height as a function of the tip bias. In this measurement, a feedback circuit is employed to change the height of the STM tip in order to maintain a constant tunneling current. Then, the tip bias is swept through a predetermined range of values and the change in the height of the tip is recorded.[70, 74]

This measurement can provide a measure of the local tunneling barrier. Using Eqn. 2.6, the height of the local tunneling barrier is given as

$$\phi = \frac{\hbar^2}{8m}\left(\frac{d\ln I}{dz}\right) \tag{2.10}$$

where ϕ is the local tunneling barrier, V is the the tip bias and z is the height of the STM tip. Although used early on to measure the work functions of various samples, this measurement has been superseded by other techniques such as Ballistic Electron Emission Microscopy (BEEM)[75].

Work by Pronschinske *et al.* has shown that this measurement can also serve as a indirect probe of the local density of states. It is particularly useful when imaging small nanoparticles, and molecules. In this case the system might undergo tip-induced chemical

reactions, desorption or other effects. For $I(V)$ spectroscopy, the tip would move too close to the sample. By using $z(V)$ spectroscopy, the tip-sample distance is fixed, allowing the researcher to obtain spectroscopic information without damaging the sample[74].

2.3 Experimental System

We use a Omicron ultrahigh vacuum(base pressure of 10^{-10} mbar) low temperature model STM, although all measurements are acquired at room temperature. STM tips are manufactured in house in a process that will be described shortly. The system gets power from an uninterruptable power supply, ensuring that electrical noise is at a minimum. During STM measurements, the STM stage is decoupled from the system in order to further isolate it from mechanical vibration. On top of this, our system is mounted on a table that employs active vibration isolation.

2.4 Reliable fabrication of ultrasharp STM probes for atomic resolution imaging

Regularly obtaining atomic resolution image of samples require the production of ultrasharp, mechanically stable STM tips[76]. Ultrasharp SPM probes are important for a number of other characterization methods, and so a great deal of study has gone into the development of these techniques[77]. We have evaluated a number of tip etching techniques in order to hone our method[51, 78, 79].

Our tips are made by electrochemically etching tungsten wire. Various labs use both AC and DC power supplies to etch the tips. The tips are etched in NaOH solution. Hydrogen bubbles form at the cathode. If the cathode is the tip, then bubbles will form on the tip, impeding the uniform etching. In order to come up with a uniform etch, it is necessary to use DC power, with the tip acting as the anode.

There are a number of configurations used to electrochemically etch the tip. The two most common configurations involve the submerged etch method[78, 80–82], and lamella

17

etch method[51, 79, 83, 84].

2.4.1 Methods for fabricating STM tips

In the submerged tip method, a beaker is typically filled with NaOH solution. A tin ring is hooked up to the power supply and placed at the bottom of the beaker. The tungsten wire is hooked up to the power supply, and then submerged in the NaOH solution. The solution runs up the side of the tip to provide an extended meniscus. More etching occurs at the liquid-air interface of the tip. After a certain amount of time, the bottom half of the wire will break off leaving a sharp tip. It is important to stop the etching at this point, so that the tip is not dulled by back-etching. Several methods can be employed to determine when the wire breaks in order to stop the etching. The simplest is to etch the tip for short, set periods of time. Then the progress of the etching can be monitored and minimal back-etching can occur. Other methods monitor the current flowing through the system, and employ either threshold or differential cutoffs to eliminate back-etching[78]. In our experience, the submerged tip methods are unable to regularly produce sharp tips. When the process works, the tip has an exponential shape. It is possible to exert some control of the final tip length and shape, by adjusting the amount of the submerged tungsten wire.

Lamella methods have also been employed to etch tungsten wire tips[79, 83]. In the lamella method, a gold wire ring with an 8 mm diameter is fashioned and suspended in air. The NaOH solution is suspended in the gold ring. The ring is hooked up to the cathode of the power supply, and the tungsten wire is hooked up to the anode. The wire is placed through the center of the ring, to begin etching. The practical difference between the two methods is the behavior of the meniscus. In the submerged tip method, the meniscus is static, resulting in an exponential envelope for the tip shape. In the lamella method, the limited amount of available fluid results in a dynamic meniscus shape. This means that as the wire is etched and changes shape, the meniscus shape changes as well. This results in the formation of a conical tip. Back-etching is also a concern in a single lamella method.

Several techniques can be used to minimize this effect. A differential cutoff can be used, but the current itself is noisy, making this method ineffective. It is also possible to watch the etching process, and when the bottom part of the wire falls, to manually cut the power. This, however, is a long and labor intensive process.

A third method involves adding a second lamella[79]. In the double lamella method, the upper ring is attached to the anode of the DC power supply, while the bottom ring is attached to the cathode. NaOH solution is suspended in both the upper ring, and the lower ring. The tungsten wire goes through both rings. The rings are then electrically connected through the electrolytic solution and the tungsten wire. The dominant etching occurs at the top ring. When the etching is completed, the bottom part of the tungsten wire drops down, breaking the circuit. The double lamella method then acts as an automatic cutoff for the etching.

A photograph of the tip etching station is displayed Fig. 2.3(a). The tip etching station consists of a double lamella setup, attached to a micromanipulator, and hooked up to a Keithley 2400 DC sourcemeter. The tungsten wire is mounted into a tip holder and held in place using a magnetic stand. The double lamella can then be moved relative to the tip. The entire setup is viewed under a microscope, so that it is possible to monitor the etching process. The lamella will break several times during the etching process. The microscope and micromanipulator can be used to ensure that the meniscus etches the same spot on the wire. A close up of the double lamella photograph is displayed Fig. 2.4(b). A schematic of the setup can be seen in Fig. 2.3(c). A schematic of just the double lamella can be seen in Fig. 2.3(d).

2.4.2 Evaluation of STM tips

We evaluated the tips by using them to take data (Fig. 2.4). For evaluation purposes, we attempted to obtain atomic resolution images of highly oriented pyrolytic graphite (HOPG). HOPG is a low cleavage energy system, so it is easy to create large, atomically flat surfaces.
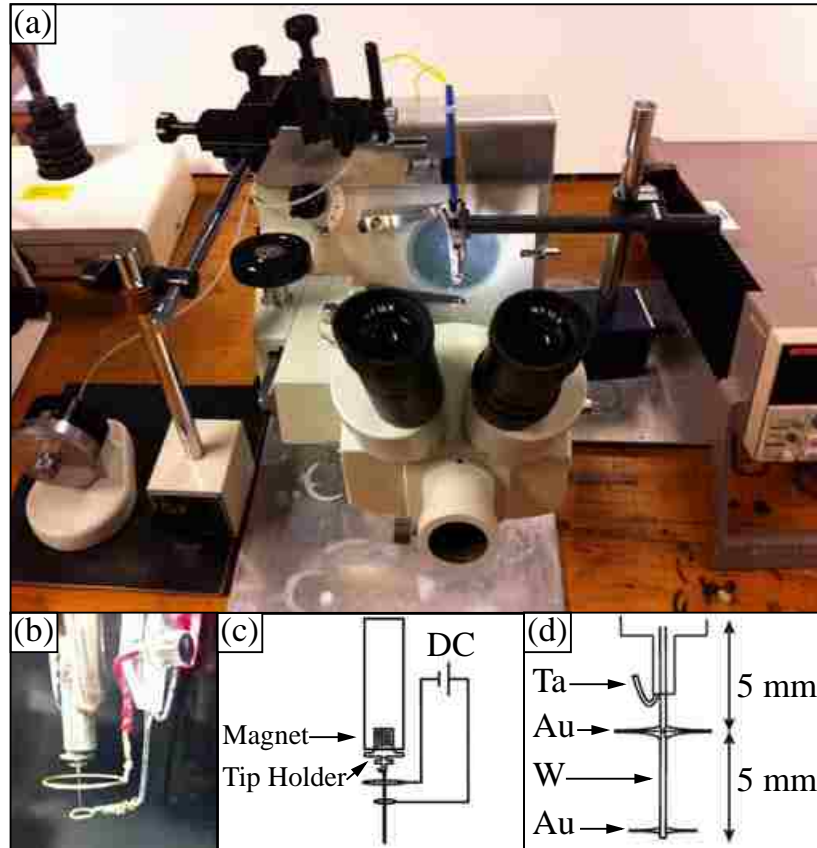
Figure 2.3: (a) Photograph of the entire tip etching setup. The tungsten wire is held in place by a magnet, while the gold, wire can be adjusted using a micromanipulator with coarse x, y, z control as well as fine z control. The setup is powered by a Keithley 2400 sourcemeter and can be viewed under magnification using the microscope. (b) Closeup photograph of the tungsten wire and the two gold loops. (c) Simple schematic describing the double lamella setup. (d) Closeup schematic detailing the position of the gold rings with respect to the tip holder. (Photographs courtesy of Dr. Paul Thibado. Used with permission.)

Then we evaluated the shape of the tip as viewed under $1000\times$ magnification. We wanted to come up with a quick and dirty method for predicting the quality of the tip before putting the tip into the STM. We settled on looking at the cone angle of the tip. The results of the study are shown in Fig. 2.4.

We evaluated the images by sorting them into three broad categories. Sample images can be seen along the right-hand side of the image. The top quality tips are capable of atomic resolution imaging of the HOPG surface. Each individual atom can be identified in the image. The next tier of images show atomic scale features, although there is not atomic resolution. In the sample image provided, we can see rows of atoms. The last tier of images does not show anything at the atomic level. These tips are only useful for imaging larger features. The corresponding sample image shows a 500 by 500 nm image of the HOPG surface. The image is largely flat, with only a single step, running diagonally from the bottom left-hand corner to the top right-hand corner.

The tips are also categorized by cone angle, so that we have tips less than $10°$, 10-20° and greater than $20°$. The chart then displays the likelihood of obtaining a quality STM image. To read the chart, pick a cone angle. Above the cone angle, are the percentage of tips that produced images of the quality of the image to the left. For example, for a cone angle between 10 and $15°$ will produce a low quality images 20% of the time, medium quality images 60% of the time, and high quality images 20% of the time.

We found that tips with larger cone angles (> 20 °) produced high quality images 70% of the time. A large cone angle, then was a good indicator of the quality of the tip. The reason for this relationship is apparent. The electrochemical etching seem to universally produce ultrasharp tips. Then to produce quality images, we need to consider the mechanical stability of the tips. If we imagine the atoms as spherical balls, we can generate a model for the ideal, mechanically stable atomically sharp tip. Such a model is shown in the corner of Fig. 2.4. Such a tip would have a cone angle of $\sim 60°$.

	0-10°	10-15°	>15°
	10%	20%	70%
	20%	60%	20%
	70%	20%	10%

20 nm

60°
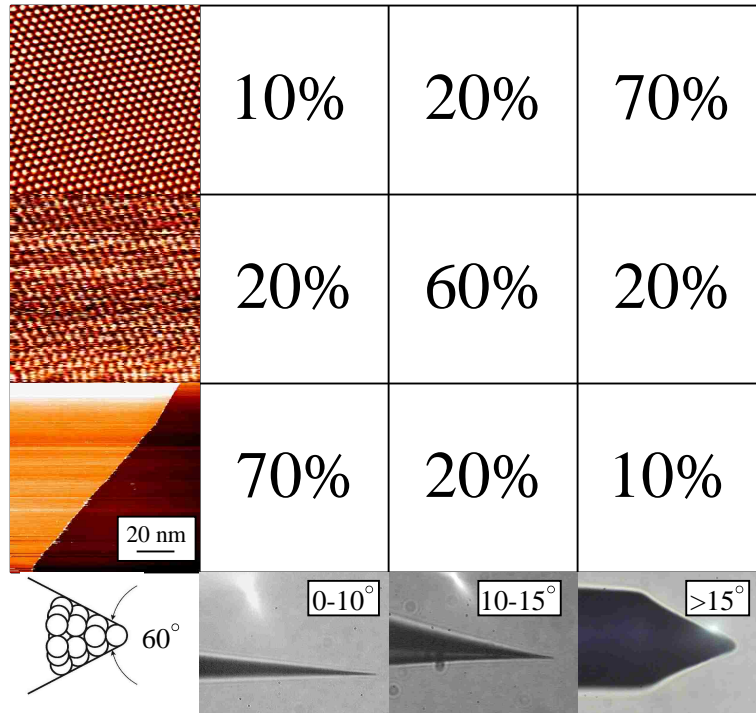
Figure 2.4: This chart relates the cone angle of a given STM tip to the quality of STM images generated by this tip. In the bottom-left corner, is a 6 nm × 6 nm atomic resolution image of the HOPG surface. Along the vertical axis are a series of filled state, constant current STM images acquired with tip bias of 0.1 V and setpoint current of 0.1 nA. The top two images show 6 nm×6 nm images of the HOPG surface. The topmost image shows atomic resolution, while only atomic scale features such as rows can be seen in the next image. Beneath these images is a large scale (100 nm × 100 nm) image of the HOPG surface. In this image, we can see a single step running from the bottom righthand corner of the image to the top lefthand image. Along the bottom axis are a series of photographs of STM tips taken with a magnification of 1000×. These tips are representative of the labeled cone angle range. The percentages give the chance that a given cone angle range will provide the specified image quality.

Chapter 3

Scanning tunneling microscopy studies on freestanding graphene

The discovery of graphene was made even more exciting when mechanical distortions were found to alter its electronic properties. For example, when a uniaxial strain is applied to the honeycomb lattice, it affects the hopping probability for electrons in the p_z orbitals. The resulting energy change can be represented mathematically by a position-dependent vector potential, as described by Castro Neto *et al.*, thereby suggesting the presence of a magnetic field[5, 85]. Further analysis clarified that it is in fact a pseudo-magnetic field because opposite Dirac cones are shifted in opposite directions in order to preserve global time-reversal symmetry. Guinea *et al.* explained that this field should, nevertheless still have a measurable impact[24]. Verification came from Levy *et al.* who grew graphene on a Pt substrate[25]. After cooling to ∼7.5 K, the graphene formed triangular nanobubbles due to its negative thermal expansion coefficient[86]. Scanning tunneling spectroscopy (STS) was then performed on the nanobubbles, and a series of peaks were attributed to Landau levels originating from static pseudomagnetic fields with magnitudes as high as 300 T.

Scanning tunneling microscopy has been a particularly powerful tool for generating and studying the strain in suspended graphene membranes[14, 47–49, 87]. In early 2012, Zan *et al.* managed to obtain atomic scale images of suspended graphene membranes, and their ripple structures. At the same time, Xu *et al.* used the electrostatic attraction between the STM tip and the sample to pull on the graphene, and generate strain on an atomic scale[47]. A backgated, suspended graphene sample was studied by Klimov *et al.*. They were able to show that the deformed graphene membrane acted like a quantum dot[49]. A particularly
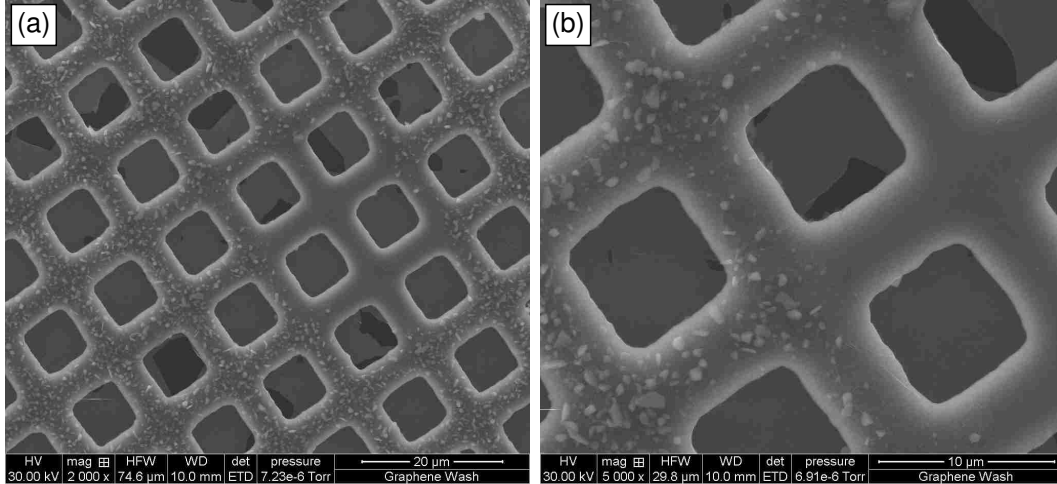
Figure 3.1: (a) SEM image of graphene mounted on a TEM grid consisting of copper bars 7.5 μm wide, and holes 5 μm wide. (b) Closeup of the same image.

interesting study by Eder *et al.* involved the study of freestanding graphene membranes using a two-tip STM, with the tips arranged on either side of the graphene membrane which allowed them to cause deformations with one tip, and image the membrane with the other[87].

In this chapter we explore the effects of a biased STM tip brought near a suspeded graphene membrane. The atomic corrugation is measured, and determined to be a function of the scan speed. This is due to an electrostatic attraction between the suspended graphene sample, and the biased STM tip. This attraction can be dramatically illustrated by sweeping the tip bias over a predetermined range while maintaining a constant tunneling current and measuring the resulting height of the STM tip. These measurements show that the graphene membrane is moving under the influence of the STM tip. This movement should result in the formation of time dependent pseudomagnetic fields.

3.1 Sample preparation details

Our graphene samples were provided by a commercial provider[88]. Graphene was grown using chemical vapor deposition[32], then transferred onto a 2000-mesh ultrafine copper grid. This grid consists of a lattice of square holes 7.5 μm wide and bar supports 5 μm wide,

24

giving suspended graphene. For the comparison purposes, we also looked at graphene on a copper foil substrate. All samples were mounted onto flat tantalum sample plates using silver paint and transferred through a load-lock into the STM sample chamber, where they were electrically grounded for all experiments.

Scanning electron microscopy (SEM) images of the graphene on the TEM grid are shown in Fig. 3.1. Fig. 3.1(a) shows large scale image. The lighter areas indicate the presence of the graphene membrane, while the darker areas indicate an absence of graphene. From these images we estimate ∼90% coverage.

STM data were acquired using tips manufactured in-house by electrochemical etching of polycrystalline tungsten wire, using a custom double lamella setup with automatic gravity switch cutoff[51] as discussed in the previous chapter. After etching, the tips were gently rinsed with distilled water, briefly dipped in a concentrated hydrofluoric acid solution to remove surface oxides[89] and loaded into the STM chamber.

3.2 Atomic scale imaging

Taking atomic scale STM data on suspended graphene samples is not easy, as the unsupported membrane is often very floppy(Fig. 3.2(a)). However, it is possible to find regions that have a static configuration [47, 48]. A typical constant current, filled state image of suspended graphene, measuring 6 nm × 6 nm, taken with a tip bias of 0.1 V and a setpoint tunneling current of 1.0 nA is displayed in Fig. 3.2(b). The image is displayed with a 4 nm black to orange to white color scale. A honeycomb pattern can be resolved throughout the image, although it is a little blurry. The image shows an overall curvature, with ridge running from the bottom left-hand corner of the image to the top right hand image.

Four line profiles, taken from a series of STM images acquired with a tip bias of 0.1 V and a setpoint current of 1.0 nA, can be seen in Fig. 3.3(a). Each line profile was acquired with different scanning speed, and they have been offset for clarity. From top to bottom, the scan speed used to acquire the image was 71.4 nm/s, 34.9 nm/s, 18.0 nm/s and 9.0
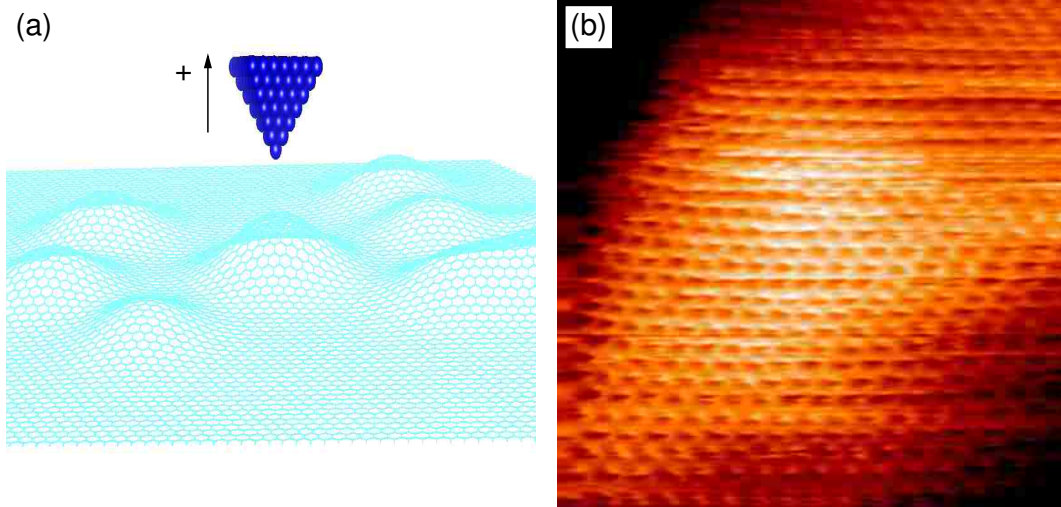
Figure 3.2: (a) Cartoon showing an STM tip near a suspended graphene membrane. (b) Constant current filled state STM image of suspended graphene measuring 6 nm × 6 nm, taken with $V = 0.1$ V and $I = 1.0$ nA. The image is displayed using a 4 nm black to orange to white color scale.

nm/s. Each line profile shows an oscillating function with the wavelength of the oscillation determined by the spatial periodicity of the honeycomb structure (around 0.3 nm). As the scan speed decreases, the amplitude of the line profile increases, from 0.13 nm for a scan speed of 71.4 nm/s to an amplitude of 1.56 nm for a scan speed of 9.0 nm/s.

Using the scan speed, combined with the wavelength (0.3 nm), we can plot the time trajectory of the STM tip, as shown in Fig. 3.3(b). The topmost line profile, since it was taken with the highest scan speed takes the shortest time to complete. The tip oscillates at a frequency of 220 Hz. As the scan speed decreases, the time needed to complete the line profile increases, and the frequency increases. From top to bottom the frequencies are given as 220 Hz, 108 Hz, 56 Hz, and 28 Hz.

3.2.1 Discussion

In addition to the frequency control, this method suggests a way to control the amplitude of the oscillations as well. An amplitude of 0.05 nm is to be expected due to changes in the local density of states over atoms, and over holes[90]. The rest of the movement is an
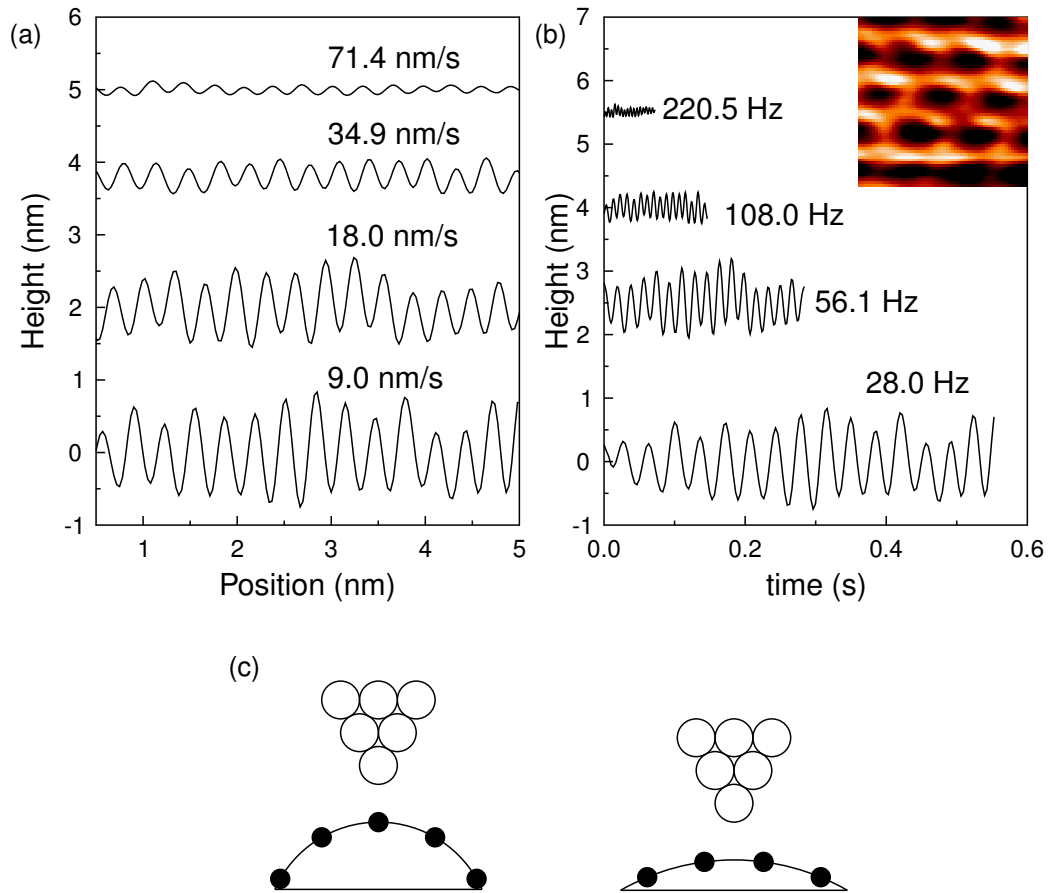
Figure 3.3: (a) Line profiles taken from 12 nm×12 nm, constant current filled state STM images acquired with a setpoint tunneling current of 1.0 nA and a tip bias of 0.1 V. The line profiles were acquired using different scan speeds, as indicated in the figure. (b) The same line profiles as in part (a) divided by their respective scan speed converts the x-axis to time. (c) Schematic showing the tip as it scans over a (left side) atom and (right side) hole.

artifact of the fact that the graphene is suspended, and thus has no bulk, as illustrated in the cartoon in Fig. 3(c).

When a biased STM tip is brought near the STM sample, there is an electrostatic attraction between the tip and the sample[12, 47, 91]. When taking constant current STM images, feedback electronics monitor the tunneling current in order to verify that it is close to the setpoint value. Suppose the STM tip is directly over a carbon atom, as picture on the lefthand side of Fig. 3.3(c). There is an electrostatic interaction between the tip and the sample, causing the graphene sample to move towards the tip. This decrease in the tip sample separation results in an increase in the tunneling current. So the feedback electronics kick in and pull the tip away from the sample. This continues until the electrostatic attraction between the tip and the sample is balanced by the elastic restoring force.

As the STM tip moves over a hole, as pictured on the right hand side of Fig. 3.3(c), the electrostatic force between the tip and the sample decreases. The graphene sample falls away from the tip, causing the tunneling current to decrease. The feedback electronics send the tip downwards towards the sample, until a new equilibrium is reached. This mechanism results in enhanced corrugations while imaging the graphene sample.

It can also explain the dependence of the amplitude of oscillation on the scan speed. For small scan speeds, the system has plenty of time to find equilibrium before the tip moves away. This results in larger corrugations. As the scan speed is increased, there is less time to establish equilibrium before the tip moves, resulting in smaller corrugations.

3.3 $z(V)$ measurements

Low frequency oscillations can be achieved using $z(V)$ spectroscopy. In $z(V)$ spectroscopy, the tip bias is swept over a predetermined range, while feedback electronics are employed to maintain the tunneling current at particular setpoint value. In order to maintain this setpoint, the STM tip must retract. The results are then analyzed by mapping the STM tip height as a function of the tip bias. For a stationary sample, this process indirectly probes

the local density of states[74, 92, 93]

$z(V)$ spectroscopy on a freely suspended graphene membrane has a different effect. Four $z(V)$ curves were acquired back to back, using a setpoint current of 1.0 nA, and ramping the tip bias from 0.1 V to 3.0 V. The results are displayed in Fig. 3.4(a). All four curves show the same basic characteristics. As the tip bias is ramped to 1 V, the height of the STM tip increases by 25 nm. As the tip bias continues to increase from 1-3 V, the tip retracts another 5 nm. The tunneling current as a function of the tip bias for one of the curves is plotted in the inset. Ensuring that that the tunneling current remains at the setpoint value means that the tip is faithfully tracking the motion of the graphene membrane.

The curves are plotted as a function of time using the fact that the tip bias ramps at a rate of 2.04 V/s in Fig. 3.4(b). This yields a saw tooth wave form with a period of 1.42 s, yielding a frequency of 700 mHz. This frequency could be tuned by adjusting the rate of the tip bias ramp. The amplitude of the wave can be adjusted by changing either the range of the tip bias ramp, or even the tunneling current[47].

3.3.1   Discussion

A cartoon, showing the effect of the $z(V)$ measurement is shown in Fig. 3.4(c). When the biased STM tip is brought near the suspended graphene sample, it induces an image charge in the sample. This leads to an electrostatic attraction between the graphene and the STM tip. As the tip bias increases, the electrostatic force increases as well. Since the graphene is freely supported, this causes the graphene to move towards the tip, reducing the tip-sample distance and increasing the tunneling current. The feedback electronics then move the tip backwards in order to maintain the setpoint current value. The tip continues to pull on the graphene membrane, but the displacement of the graphene results in a growing elastic force.

We can model the electrostatic attraction between the tip and the sample using a sphere-plane model[91, 94]. In this model, the biased STM tip is modeled as perfect sphere (similar to Ref. [95]) while the grounded graphene sample is modeled as a grounded plane. The

electrostatic field in this model can be evaluated using the method of images. We start by placing a sphere of radius a, a distance d away from the grounded conducting plane, as shown in Fig. 3.4(d) By replacing the conducting sphere at a potential V, with a point charge of magnitude

$$q_0 = 4\pi\epsilon_0 aV \tag{3.1}$$

located at the center of the sphere, we can replicate the boundary conditions at the surface of the sphere. However, this configuration will not meet the boundary conditions of the grounded, conducting plane. To correct for this, we place a second charge of equal but opposite in sign, at $-a - d$. Now the boundary conditions at the plane are correct, but the conditions at the surface of the sphere are incorrect. To fix this a third point charge is placed in front of the sphere in order to give the correct boundary conditions. This process is repeated, giving an infinite series of charges such that the ith charge is given by

$$q_i = \frac{a}{x_0 + x_i} q_{i-1} \tag{3.2}$$

The location of the ith point charge is given by

$$x_i = x_0 - \frac{a^2}{x_0 + x_i} \tag{3.3}$$

This infinite series of charges can replicate the boundary conditions, making it possible to calculate the potential, and electric field at any point. Because the magnitude of the point charges decrease with the length of the series, it is possible to use a finite number of terms to match the boundary conditions to within some acceptable error amount.

The energy of this charge configuration is given by

$$U = \frac{1}{2}\left(q_0 + \sum_i q_i\right)V \tag{3.4}$$

By taking the derivative we can then calculate the electrostatic force between the tip and
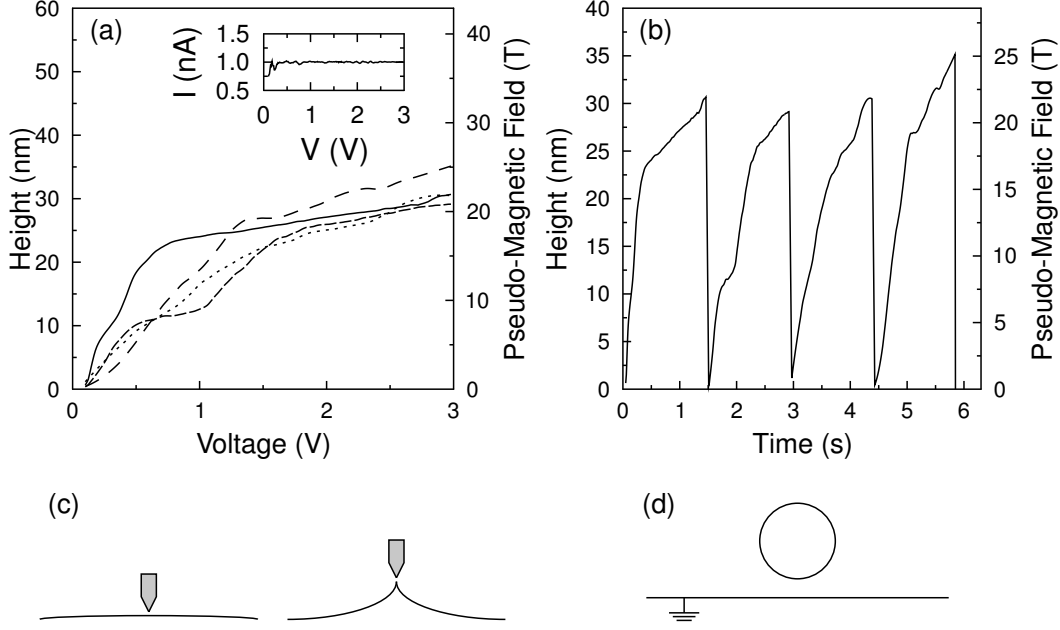
Figure 3.4: (a) Four $z(V)$ curves taken with a setpoint current of 1.0 nA. These curves were acquired sequentially. (b) Knowing that the tip bias was increased at a rate of 2 V/s, the $z(V)$ curves from (a) are replotted to give the tip height as a function of time. (c) A simple cartoon showing schematically the $z(V)$ measurement for low tip bias values (left side) and high tip bias values (right side).

the sample as

$$F = -\frac{\partial U}{\partial x} = -2\pi\epsilon_0 a V^2 \sum_i^N \frac{\partial s_i}{\partial} \tag{3.5}$$

where we set $s_i = q_i/q_0$. This analysis shows that the electrostatic force is proportional to the square of the tip bias.

The ability to drive the freestanding graphene in a controllable manner may be utilized to further study the relationship between the mechanical, electronic, and pseudo-magnetic fields properties of graphene. For example, in a previous study, Xu *et al.* used the analytical expressons for the deformation of a membrane from Ref. [96] along with the expressions for the pseudo-magnetic field in Ref [24] and the deformation potential from Ref. [97] to estimate the pseudo-magnetic field created by the induced strain. For this same freestanding graphene geometry and for small displacements, they found the pseudo-magnetic field varied linearly

at a rate of about 0.7 T/nm[47].

3.4 Pseudomagnetic fields

The frequency of oscillation is plotted as a function of the scan speed in a log-log plot in Fig. 3.5(a). Results from STM imaging are plotted as filled-in squares. Results from the $z(V)$ spectroscopy are shown as large empty white squares. The amplitude is shown as a function of the scan speed using the same key. The second y-axis relates the amplitude of the oscillation to the amplitude of the strain-induced pseudomagnetic field. In Fig. 3.5(c), we combine results. In a log-log plot the pseudomagnetic field strength is plotted as a function of the frequency of the driving force.

There are several fascinating points related to these results that need to be discussed. One is the relatively small displacements required to generate such large pseudomagnetic fields. This leads to fast switching times and low energy costs. Also, the large range of frequency and amplitude control provides access to numerous ways to test and modify experimental outcomes. It is also possible to consider using these dynamic field effects near defects and edges already present in freestanding graphene, in order to test if time-reversal symmetry may be broken, which is an important basic physics question for massless, Dirac fermions[98].

3.5 Summary

In summary, we have shown the significant effects that can occur when an STM tip is brought into close proximity with a freestanding graphene membrane. During the STM imaging process we observe an enhanced atomic corrugation caused by the electrostatic attraction between the tip and the sample. This electrostatic force can be exploited using the $z(V)$ measurement, in order to pull on the graphene sample. A more subtle interaction takes place by exploiting the negative coefficient of thermal expansion for graphene. By heating the graphene using the tunneling current we are able to generate a repulsive thermal load. By exploiting these two techniques it is possible to carefully tune the strain in a freestanding
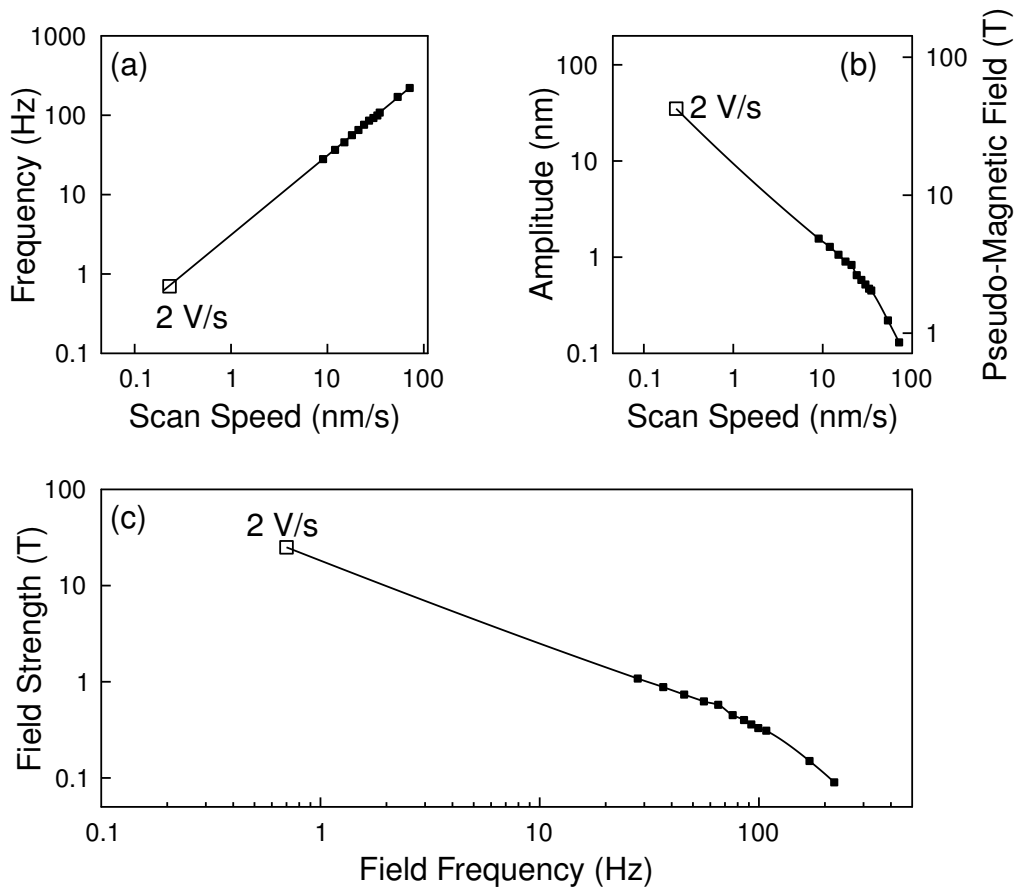
Figure 3.5: (a) Frequency of oscillation for the graphene membrane displayed as a function of the STM tip scan speed.(b) Amplitude of the oscillation for the graphene membrane displayed as a function of the STM tip scan speed. The amplitude of the height oscillations is also proportional to the amplitude of the pseudomagnetic field. (c) Maximum values of the pseudomagnetic field are plotted as a function of the frequency of the oscillations.

graphene membrane.

Chapter 4

Thermal mirror buckling in freestanding graphene membranes induced by a scanning tunneling microscope tip

Being only a single atom thin, and possessing record-breaking electron mobility, graphene shows great potential in the field of flexible electronics. Many important nanoelectromechanical (NEM) graphene device concepts have been recently developed based upon the electromechanical properties of graphene. For example, Chen *et al.* demonstrated that graphene can be used as a nanomechanical resonator with an electrical readout that varied with temperature or added mass[99]. Shortly after, Park *et al.* demonstrated a graphene mechanical actuator. This actuator consisted of a bilayer paper, with multiwall carbon nanotubes on one side, and graphene oxide platelets on the other. At low humidity, the paper would curl up. As the humidity was increased, the paper would first flatten, and then curl in the other direction.[15].

Scanning probe microscopy has been a particularly useful tool for studying NEMS device applications. One such study, performed by Mashoff *et al.* involved imaging a rippled graphene membrane on a SiO_2 substrate. By changing the imaging conditions, these researchers were able to cycle the ripples through two positions, separated by a height of almost 60 pm[100]. Larger effects can be seen on suspended graphene membranes. One such study, carried out by Lindahl *et al.*, looked at prebuckled graphene membranes. By generating large electrostatic forces, they were able to use a snap-through instability, to get a fast, $\sim$50 nm movement in the graphene membrane.[101]. The most recent development was by Eder *et al.* where they placed an STM tip on either side of a freestanding graphene

film and demonstrated tunable membrane deformations using electrostatic control[87].

Thermal actuation provides a promising avenue for further research. Thermal actuation of a microelectromechanical device (that is silicon on insulator technology) was first introduced because thermal loads provide a significantly larger force as compared with electrostatic actuation[102].

Heating under the STM tip has been studied experimentally and a giant enhancement in electronic tunneling at higher energies due to an intrinsic phonon mediated inelastic channel was found to be responsible for an unexpected gap-like feature in the graphene tunneling spectrum[103]. Progress with theoretical estimates for the heating have also been made by studying inelastic currents through nanoscale molecules sandwiched between gold electrodes, for example, refs [104, 105].

In this chapter, control over the local height and curvature of freestanding graphene is demonstrated by varying the STM tunneling current. This movement of the graphene membrane can be tuned to vary smoothly or in step-like jumps attributed either to electrostatically induced mirror buckling or to tunneling current induced (that is, thermally induced) mirror buckling. The observed thermal buckling is explained by both elasticity theory and large-scale molecular dynamics (MD) simulation. Standing on the body of work and combining with our discovery of negative thermal buckling, we propose an electro-thermal-mechanical (ETM) device.

4.1   Z(I) Measurements

We will start by introducing a simple measurement. In this measurement, the STM tip is brought near a suspended graphene sample, and a potential bias is applied between the tip and the sample in order to facilitate electron tunneling. The setpoint tunneling current will then be swept over a predetermined range, in this case 0.01-20.0 nA. During this measurement, the feedback electronics of the STM are left on, so the height of the tip is adjusted to maintain the specified setpoint current. This measurement is conducted at room

temperature.

Using simple tunneling theory we can predict the result of this measurement. In order to increase the tunneling current while maintaining a constant tip bias, the STM tip must move inwards towards the sample. However, recall from Chapter 2 that moving the tip inwards a single angstrom should result in a factor of 10 increase in the tunneling current. So the tip should move inwards, but only a very small amount.

This experiment has been carried out on two different samples and the results are shown in Fig. 4.1. The first sample is graphene on a copper foil substrate[32], while the second is graphene suspended on a TEM grid as described in Chapter 3. For this plot, a positive displacement corresponds to the STM tip moving away from the sample, while a negative displacement corresponds to the tip moving towards the sample. For the graphene on copper sample, the STM tip undergoes a small displacement of -3 nm as the setpoint current is ramped to 20.0 nA. This is consistent with our expectations as discussed above.

The suspended graphene sample is different. As the setpoint current increases from 0.01 nA to 7 nA, the STM tip moves inwards to the sample a distance of 20 nm. As the setpoint current continues to increase, the the average height remains constant, although the tip undergoes thermal fluctuations around this minimum value. Simultaneously with this measurement, the actual tunneling current was measured in order to verify that it was matched the specified setpoint tunneling current. The tunneling current is plotted as a function of the setpoint current and displayed in the inset of Fig. 4.1.

This 20 nm displacement is much too large to be explained by the simple tunneling theory mechanism described above. Instead, we conclude that this measurement is a result of the negative coefficient of thermal expansion for graphene[86, 106]. As graphene is heated[107], the out of plane modes increase in amplitude, bringing in the edges of the graphene membrane, and causing the sample as a whole to contract rather than expand[108]. For our measurement, when a potential bias is applied to the tip-sample system, an electrostatic attraction causes the graphene membrane to be pulled up towards the tip. The increase in
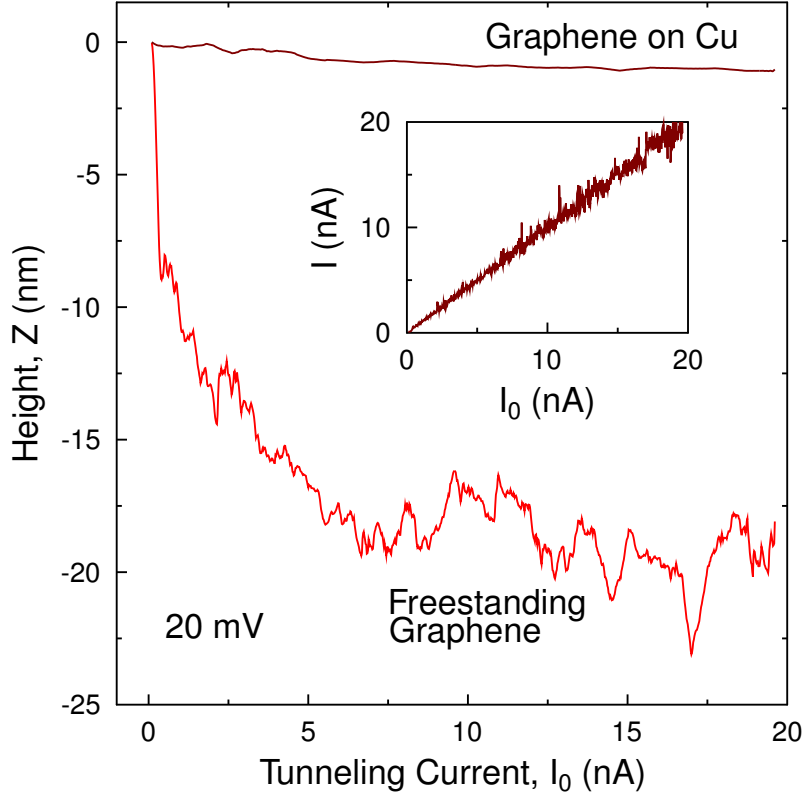
Figure 4.1: Tip height plotted as a function of the setpoint current for graphene on copper as well as freestanding graphene sample. Actual Tunneling current as a function of the setpoint current is displayed as an inset.

the tunneling current during the $z(I)$ measurement locally heats the graphene membrane. Due to the negative coefficient of thermal expansion, this results in the graphene membrane contracting away from the tip. In order to achieve the desired setpoint value, the tip chases the graphene membrane. Therefore the full 20 nm movement is due to a physical movement of the graphene sample.

4.1.1   Estimating the temperature increase due to the tunneling current

It is surprisingly difficult to estimate the local heating due to the tunneling current from an STM tip. An early STM study used the tunneling current to melt nanostructures on metal surfaces with known melting temperatures. However, when they used classical heat diffusion theory they found that in order to generate the proper power to melt the material, it was
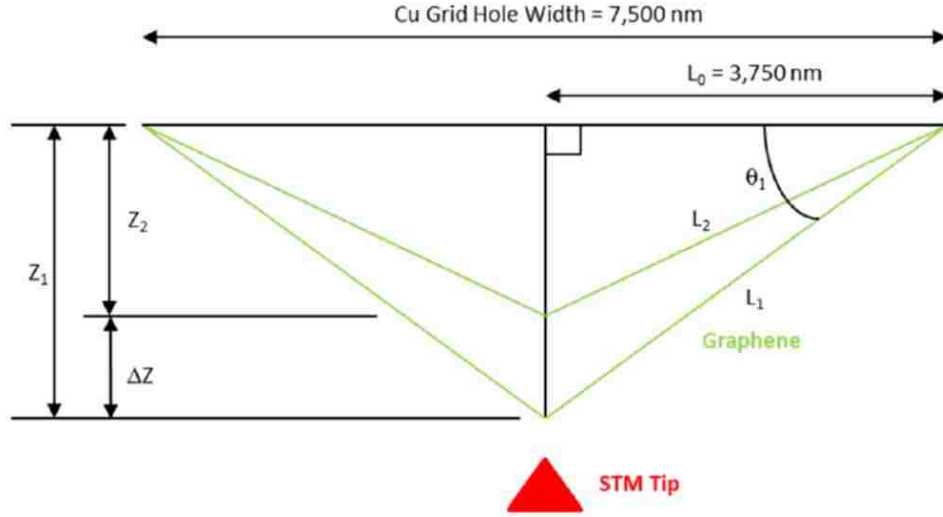
Figure 4.2: A simple model of the sample showing the contraction of the graphene membrane during the $z(I)$ measurement. From this model, along with the value for the coefficient of thermal expansion for graphene, α, we are able to estimate the temperature increase being between 10-150 K

necessary to assume a mean free path for electrons that was smaller than the interatomic distances[69].

Instead of directly calculating the temperature, we can obtain an estimate of the temperature increase from the observed contraction during the $z(I)$ measurement. Bao *et al.* used a similar setup to calculate the coefficient of thermal expansion for graphene for a large range of temperatures[86]. These research suspended graphene over Si trench. They then measured the change in the length of the graphene over the trench. Using this method, they obtained an estimate for the coefficient of thermal expansion at room temperature to be -7×10^{-6} K^{-1}. Using this number, as well as the contraction of the graphene membrane calculated above, we can now estimate the increase in temperature due to the tunneling current as

$$\Delta T = \frac{1}{\alpha} \left(\frac{\Delta L}{L_0} \right) \tag{4.1}$$

A cartoon, showing the geometry of the graphene sample is shown in Fig. 4.2 so that

	Example 1	Example 2	Example 3
$\alpha(1/\mathrm{K})$	-7.0×10^6	-7.0×10^6	-7.0×10^6
$L_0(\mathrm{nm})$	3750	3750	3750
$\Delta Z(\mathrm{nm})$	20	20	20
$\theta(°)$	11.0	5.50	0.70
$Z_1(\mathrm{nm})$	729	361	46
$L_1(\mathrm{nm})$	3820	3768	3752
$Z_2(\mathrm{nm})$	709	340	24
$L_2(\mathrm{nm})$	3816	3765	3752
$\Delta L(\mathrm{nm})$	-3.77	-1.94	-0.2
$\Delta T(\mathrm{K})$	144	71	7.8

Table 4.1: This table lays out the possible changes in temperature given different geometries for the suspended graphene.

we can calculate the relative change in length of the sample. The graphene hangs down in the hole of the TEM grid (first described in Chapter 3) characterized by an unknown angle θ. The width of the hole of the TEM grid is 7.5 μm. From the width of the hole, as well as the hanging angle, we calculate the initial height of the graphene membrane as $z_1 = (3750 \text{ nm}) \tan \theta$. After contraction, the height of the graphene sample is given by $z_2 = z_1 - 20$ nm. From these numbers we can calculate the relative change in the length of the graphene membrane before and after contraction. Since we do not have a way to measure the initial hang angle θ we calculate possible temperature calculations for a range of angles, $\theta = 11°, 5.50°, 0.70°$. From these values we can conclude that that the increase in temperature due to Joule heating is around 10-150 K.

4.2 Thermal Mirror Buckling in Graphene

Next, we will combine the $z(V)$ measurements discussed in Chapter 3, with the effects due to the tunneling current. In order to do this, two sets of $z(V)$ curves are obtained. For the first set of $z(V)$ measurements, the tip bias is swept over a range of 0.1-3.22 V for various setpoint tunneling currents. In the second set of data, the tip bias is swept from -0.1 to -3.1 V. Changes in the tip height are recorded as a function of the tip bias.

For each setpoint current value, ten $z(V)$ curves are obtained and averaged together. The results of these measurements are displayed on the righthandside of Fig. 4.3(a). For clarity, only six characteristic curves have been shown-three positive tip bias sweeps and three negative tip bias sweeps. For low setpoint current ($I = 0.1$ nA), the curves are very similar to those seen in the previous chapter. As the tip bias is increased to 1 V, the height of the tip increases by 30 nm. After this, the tip height increases at a much slower rate and eventually plateaus. This measurement is entirely reversible. As the setpoint current is increased to 0.2, 0.5, 1.0, 2.0 and 3.0 nA, the $z(V)$ measurements are qualitatively similar (measurements not shown here).

Increasing the setpoint current beyond this mark leads to an interesting effect. A $z(V)$ curve, taken with a setpoint current of 4.0 nA, is shown just above the $z(V)$ curve that was taken as 0.1 nA. This curve, unlike the others in the figure, is a single measurement, and not an average. As the tip bias is ramped from 0.1-1.0 V, the height of the tip increases by 45 nm. As the tip bias is increased further, little to no movement is seen in the height of the graphene membrane. Then, at a tip bias of 3.0 V, the height suddenly increases by ~ 40 nm. Then the height of the tip falls slightly. $z(V)$ measurements taken after this measurement show very little movement. A typical high current measurement is displayed above the 4.0 nA curve. This curve is taken with a setpoint current of 10.0 nA. As the tip bias increases during this measurement, the height of the STM tip increases by 3 nm.

Of course, during these measurements it is important to monitor the tunneling current in order to make sure that it stays near the setpoint value. During the acquistion of the critical $z(V)$ curve ($I_c = 4.0$ nA) the tunneling current was recorded and is displayed in Fig. 4.3(b) as function of the tip bias. During this measurement the setpoint current is nearly constant at 4.0 nA, except for at 3.0 V, when it spikes to ~ 20 nA before returning to the setpoint value. This sudden spike in the tunneling current indicates that the graphene membrane is moving faster than the STM tip can respond[70]. However, this is still less than the saturation current (50 nA) so the tip does not crash into the sample.

Topography data was taken before and after the $z(V)$ measurement. A line profile from the topography scan is shown in Fig. 4.3(c). The line profile shows that that height of the STM tip undergoes some small fluctuations in height. Two-thirds of the way through the scan, there is a large, permanent increase in height. The height after the $z(V)$ measurement is ~ 80 nm greater than before the measurement. This is illustrated in Fig. 4.3(a) by displaying the rigid $z(V)$ above the critical curve.

A second set of $z(V, I)$ curves were taken and displayed in the lefthand side of Fig. 4.3. These curves are qualitatively the same as the other set, however they have been taken by ramping the tip bias from -0.1 V down to -3.22 V. For this set of data, the critical $z(V)$ curve occurs at 2.0 nA. Because the electrostatic force between the tip and sample is due to an image, this interaction is always attractive.

4.2.1 Discussion

This large, sudden increase in the height of the graphene membrane has been observed before[87, 101], and is typically referred to as mirror buckling. This refers to a dimple in a membrane, characterized by a given radius of curvature suddenly reversing its curvature. However, these previous studies showed mirror buckling through only the application of an electrostatic force. This is not the case here, where repeated $z(V)$ measurements at low setpoint currents show that measurement is reversible. It is only after increasing the setpoint current that the buckling event occurs. This clearly indicates that the temperature plays an important role in this buckling event.

A dramatic illustration of the thermal load is demonstrated in Fig. 4.4. The previous algorithm is used to prepare the graphene membrane into a rigid state. A series of $z(V)$ curves are taken, each with increasing setpoint currents. At a critical value, the graphene buckles as before. This critical curve, displayed in Fig. 4.4(a) is interesting as it shows two buckling events.

If we look at the tunneling current as a function of the tip bias, shown in Fig. 4.4(b), we
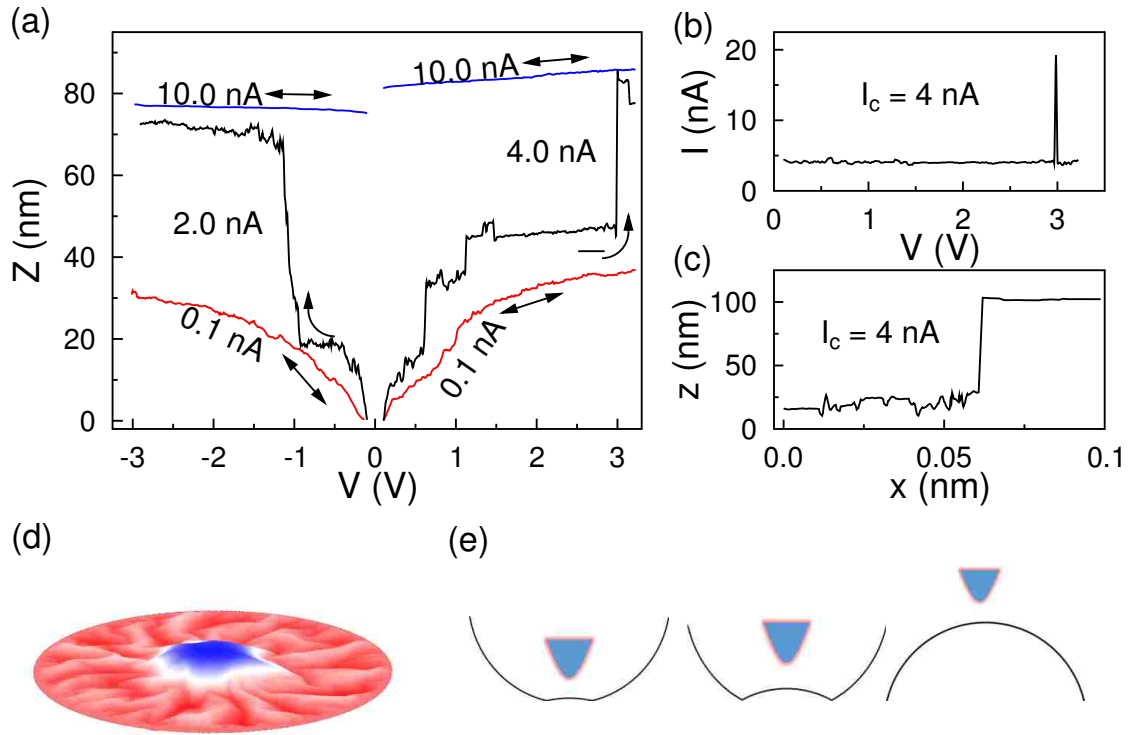
Figure 4.3: (a) Constant current $z(V)$ measurements displayed for various setpoint currents. A double arrow indicates that the measurement is reversible. (b) Tunneling current measured as a function of the tip bias acquired simultaneously with the 4.0 nA $z(V)$ curve shown in (a). (c) Topographic scan taken concurrently with the positive bias $z(V)$ curves shows a permanent increase in height. (d) Illustration of the buckled graphene membrane, after the critical $z(V)$ measurement.

see two spikes. These spikes occur at the same tip bias as the jumps. However, both events are below the saturation point for our system, so the tip does not crash.

After the graphene was prepared into the buckled, rigid state as before, as series of constant current 0.1 nm×0.1 nm images were obtained with a tip bias of 10 mV. The tunneling current was slowly increased. As the setpoint current reached 30.0 nA, the height of the STM tip remained constant. Then, almost halfway through this scan, the graphene buckled down as seen in Fig. 4.4(c). This reversed the buckling event brought about by the $z(V)$ curves. This is a definitive test that the STM tip is capable of exerting a thermal load on the graphene membrane.

4.3 Molecular dynamics simulations

In order to further explore the role of temperature in the buckling event, we had collaborators carry out molecular dynamics simulations. For the computer model, a circular graphene sheet consisting of 1.1 million carbon atoms with a diameter of 0.18μm was used. The nearly micron size of the sample was necessary because many different length scales are present in this problem, and therefore it was critical for capturing the very important behavior.

We used the AIREBO potential that is particularly well suited for simulating properties of hydrocarbon systems[109]. The circular sheet of graphene in the computational model was divided into four regions as shown in Fig. 4.5. The central region, defined for $r < 10$ nm is directly below the STM tip. This region is held at a temperature T_c, that is altered in order to model the effect of the changing tunneling current. A 0.2 nm band at the boundary ($89.8 < r < 90$ nm) is held fixed and subjected to a small shear strain (0.1%) and held fixed in space. Moving inward ($88 < r < 89.8$ nm) a small region is held at a temperature of 300 K. In the remaining region, containing the remainder of the atoms, the temperature is calculated to fit the conditions of the inner and outer regions.

In order to include the effect of the STM tip bias voltage V, we modeled the tip-sample system as a capacitor whose capacitance C is governed by the geometry of the tip-apex, as
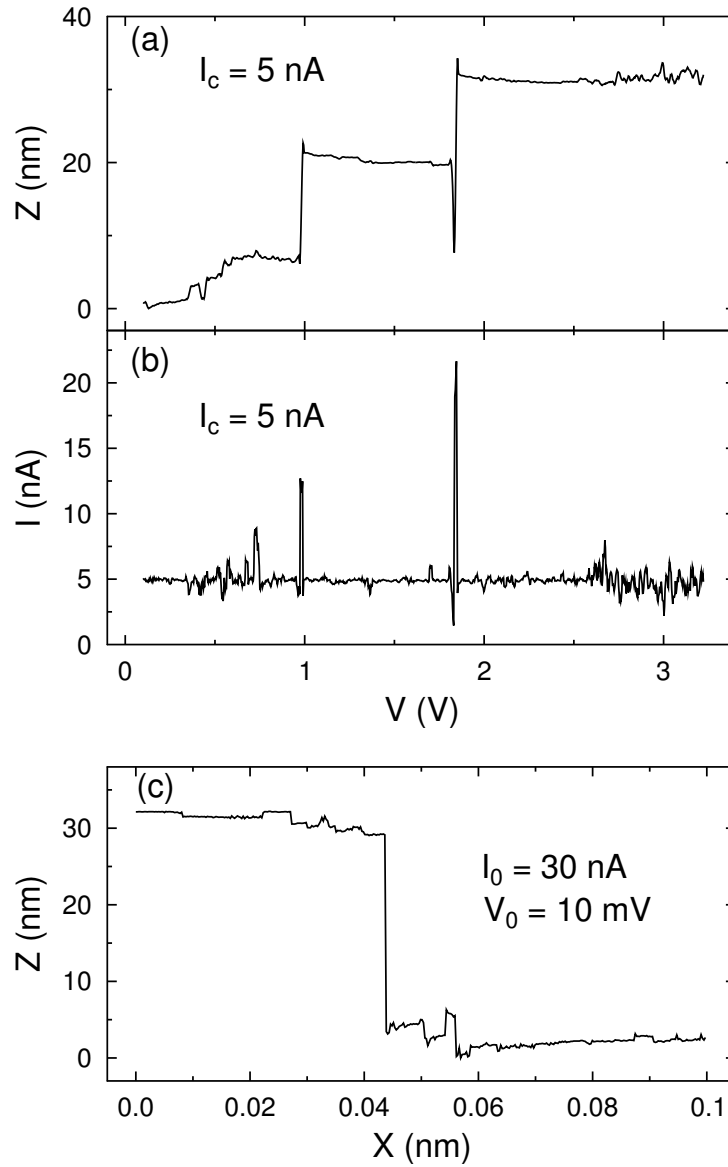
Figure 4.4: (a) $z(V)$ curve taken with a setpoint current of 5.0 nA. This curve shows two buckling events at 1 and 1.75 V (b) $I(V)$ curve taken simultaneously with the $z(V)$ data. (c) A series of topographic images of 0.1 nm × 0.1 nm size taken with increasing setpoint currents, and a tip bias of 10 mV. This is a line profile taken from the last topographic image, taken with a setpoint current of 30 nA.
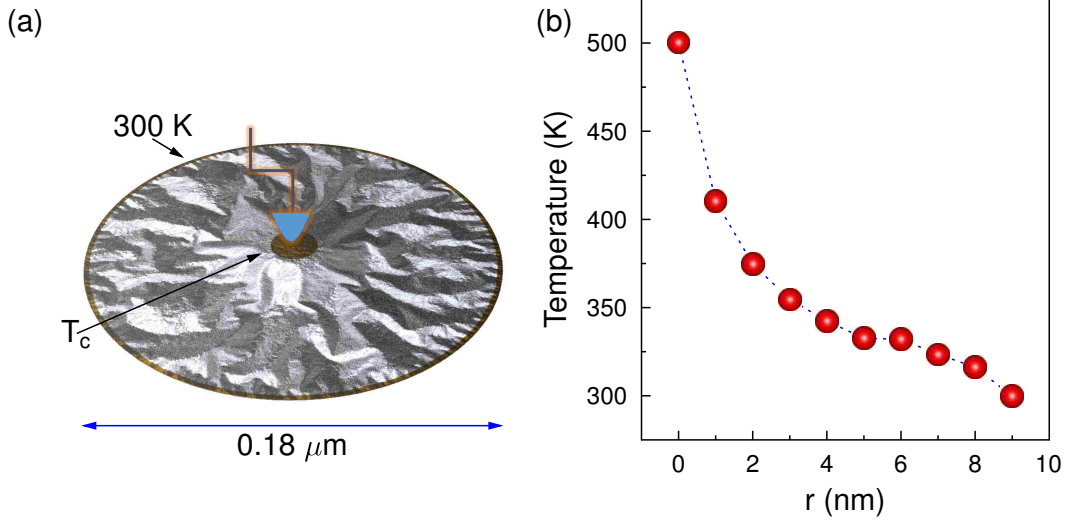
Figure 4.5: (a) The MD simulation is a circle of radius 0.9 μm, containing 1.1 million carbon atoms. It is divided up into four regions. (b) Temperature gradient for the MD simulations when the central region is held at $T_c = 500$ K and the edge of the membrane is held at 300 K.

well as the tip-sample separation. To model the tip-apex, we distributed the charge $q = CV$ according to a Gaussian distribution of width $\sigma = 10$ nm (that is, the size of the central region) over the atoms of the graphene layer, and we assumed the local electric field E is uniform over the region. Both C and E are determined by solving the boundary value electrostatic problem using a finite difference method[110]. In this way, an electric field $F_i = q_i E$ is applied normal to the surface at each atom i during the MD simulation. Since both the applied field and the atomic charges q_i are proportional to the bias voltage, the electric force is proportional to V^2.

Owing to the vastness of the system, it was also necessary to narrow the scope of the simulations. It would be impossible to simulate the entire experiment because the bias voltage is swept over two decades, the current is swept over three decades and the experiments run for hours. We focus our attention on what is new and interesting in the MD experiments, which is the role of temperature on the mirror buckling process.

A convex buckled graphene sheet was prepared by placing it under the influence of a 3 V bias, as shown in Fig. 4.3(d). The graphene height distribution for this initial state

is displayed in Fig. 4.6(a). The bias is reduced to 0.22 V, but the shape of the graphene membrane does not move, indicating that the buckled configuation is stable. Next, the temperature was increased $T_c = 500$ K. The simulation evolves for 50 ps and the resulting height density plot is shown in Fig. 4.6. This plot shows a small dimple in the center. Line profiles for both plots are extracted and shown in Fig. 4.6(c). The room temperature simulation, plotted in red, shows a peak at the center. The high temperature simulation, plotted in blue, shows that the membrane has buckled down. A closeup of the central region is shown in Fig. 4.6(d) showing the peak to decrease ~ 3 nm.

In order to confirm that the buckling effect is due to the heating, a second simulation is performed. In the second simulation, the bias is set to 0.22 V, but T_c remains at 300 K. The system is then allowed to evolve in time for 50 ps. The height of the membrane is shown as a function of time in Fig. 4.7(a). The height of the central atom is shown as a solid line, while the average height of the central region is shown as a dashed line. The results from the 300 K simulation are shown in red, while the results from the 500 K simulation are shown in green.

When T_c remains at 300 K, the height of the central region does not decrease, and, in fact, increases by 0.5 nm. Then central atom undergoes noticebly more fluctuations. When T_c is instantaneously increased to 500 K, the height of the central atom decreases from 11 nm to 7.5 nm. The fluctuations of the central atom are larger than before.

This scenario is similar to placing an STM tip above a convex graphene membrane. In this configuration, there is an attractive electrostatic force pulling the graphene membrane upwards, while the thermal load induced by heating generates a repulsive force. This results in the graphene membrane buckling away from the tip.

A more pronounced effect can be observed by placing the STM tip over a concave region as seen in the lower section of Fig. 4.7(b). In this image the tip has been placed beneath the graphene membrane in order to maintain consistency with the direction of the height change. The simulation starts with the same initial configuration. This time however, the

47
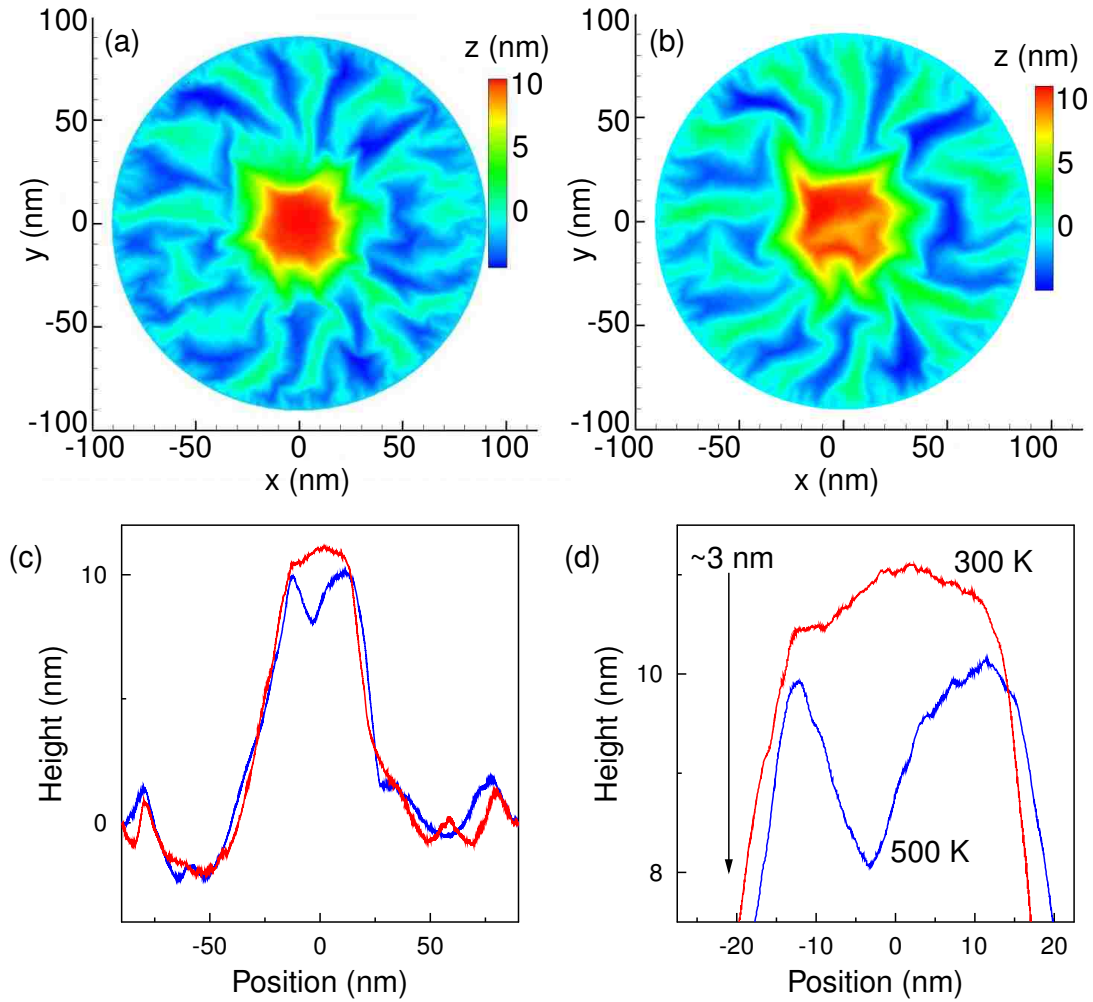
Figure 4.6: (a) Height density plot of the initial buckled configuration of the graphene membrane. The tip bias is 3 V, and the temperature of the central region is 300 K. (b) Height density plot of the graphene membrane after 50 ps of heating. The tip bias is 0.22 V and the temperature of the central region is 500 K. (c) Line profiles for the membranes in part (a) and (b), shown to highlight the buckled center (d) Closeup of the line profiles shown in (c)
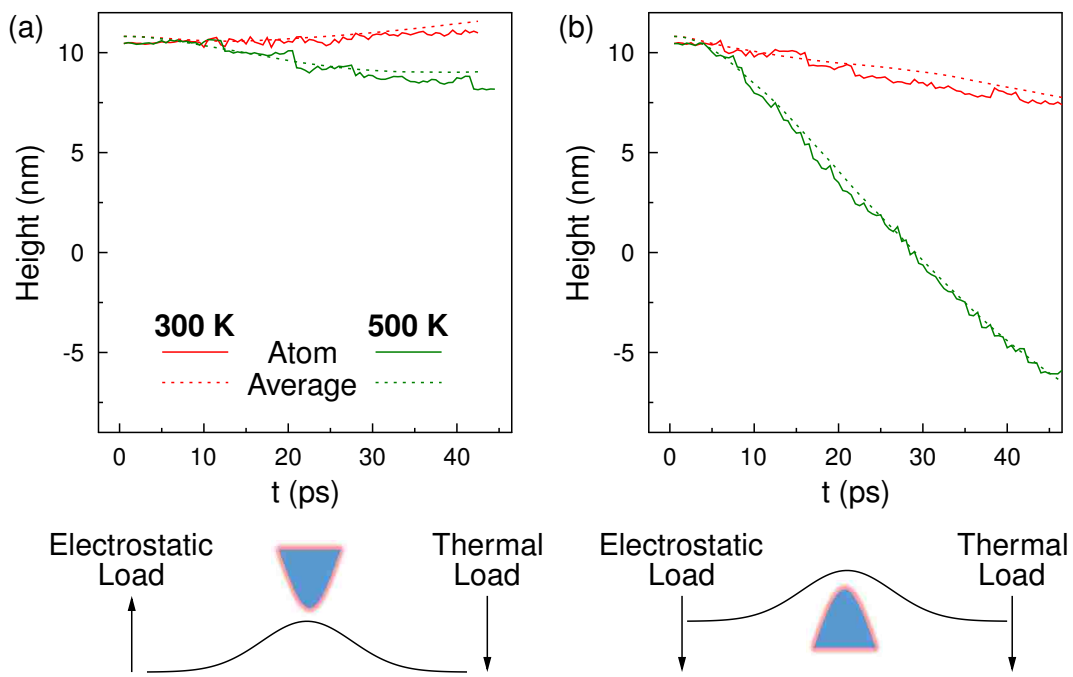
Figure 4.7: (a)Time trajectory of the average of the central region when the tip is placed over a bump. (b) Time trajectory of the average of the central region when the tip is placed over a depression.

electrostatic force is pulling the membrane down. When T_c is increased to 500 K, and the system is allowed to evolve in time for 50 ps. At the end of the 50 ps time period, the height of the central region is now negative, meaning the the ripple has flipped over. In this configuration, both the electrostatic force and the thermal load are acting in the same direction, resulting in a large, quick displacement. This is similar to the medium current curves seen in Fig. 4.3(a).

4.3.1 Discussion

These measurements show that the geometry of the graphene membrane affects the thermal load. If the STM tip is placed over a concave graphene bump, then the graphene is pulled upwards towards the tip. As the tunneling current is increased, the graphene is heated. This causes the graphene in a concave configuration to contract away from the tip. So the electrostatic force between the tip and the sample is opposed to the thermal force due to the tunneling current.

When the graphene is placed over a convex graphene configuration, the tip still has an electrostatic attraction to the sample. However, now as the graphene is heated, it again contracts, but this time buckles towards the STM tip. So the electrostatic force and the thermal load are aligned.

Now we can explain the buckling results from the STM experiment. Initially, for low tunneling current, the graphene is in a flexible reversible state. As the tunneling current is increased, the graphene contracts away from the tip. When the tunneling current is large enough, this causes the graphene to take on a convex shape. Then, on the next $z(V)$ curve, the electrostatic force and thermal load are aligned, resulting a massive buckling event.

There is a difference in the size of the jumps measured by the MD simulations and the STM experiment. However, there is also a change in the scale of the system (0.2 μm for the MD simulations, and 7.5 μm for the STM experiment). The jump in the STM experiment is an order of magnitude larger than that of the MD simulations, however, the size of the
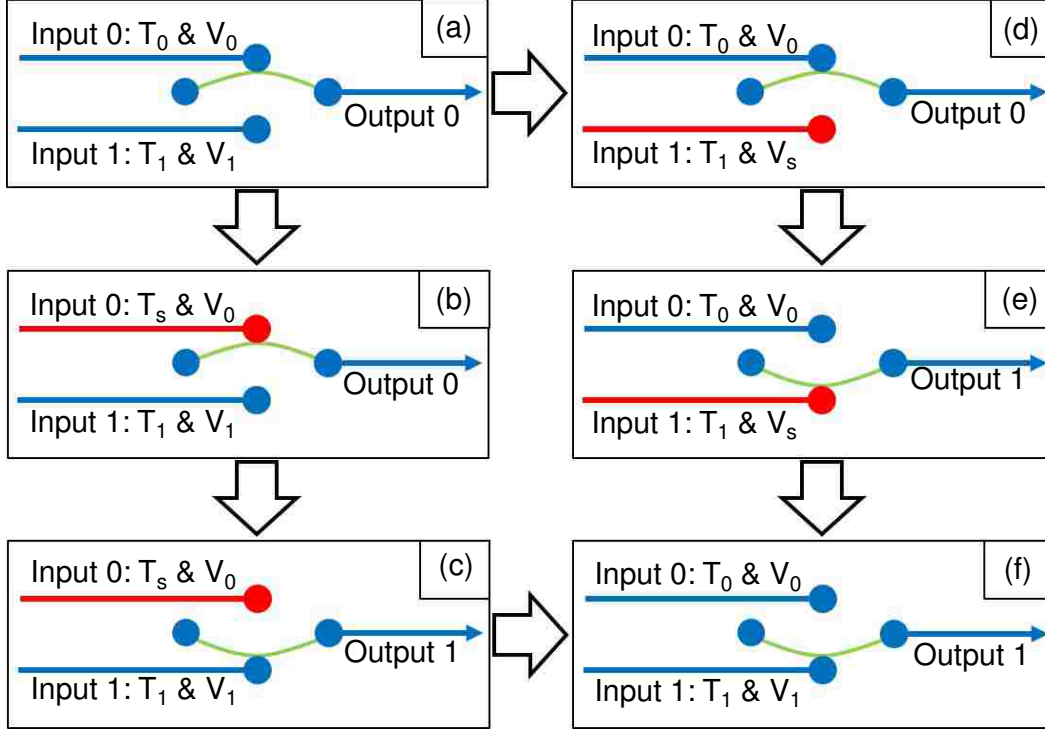
Figure 4.8: Scheme for creating ETM device using a suspended graphene membrane. Given different input configurations, the device can be in one of two states. Going from (a)-(b)-(c)-(f) shows one path for switching from input 1 to input 2, and the path described by (a)-(d)-(e)-(f) gives another.

system is an order of magnitude larger as well. There is a difference in the timescales as well. The MD simulations happen in 50 ps, while the STM experiment is on the order of seconds. However, two important points must be raised. The first is that in the MD simulations, the change in temperature is instantaneous, while for the STM experiment, it will take some finite time to heat the graphene sample. The second is that the true motion of the sample could be too fast for instantaneous tracking by the STM tip.

4.4   Electrothermal mechanical device concept

The thermal actuation demonstrated in these thermal buckling measurements, that combined with electrostatic forces could give dual electro-thermal control. This could be exploited to create a device based on electro-thermal actuation. Such a device concept is illustrated

in Fig. 4.8. The device has two inputs, denoted by input 1 and input 2. In the initial configuration, a graphene membrane, connected to the output is buckled towards one of the inputs as shown in Fig. 4.8(a). By heating the first input, the graphene buckles downwards, and connects to the second input shown in Fig. 4.8(b-c) Then the first input is cooled, and the device returns to a state identical to the first, except that the input has been switched. Alternatively we could follow a different scheme. We start with the device in the configuration shown in Fig. 4.8(a). This time, a large potential is applied to the second input (Fig. 4.8). This causes the graphene membrane to buckle downwards (Fig. 4.8). The potential bias is then removed, and then the graphene device is returned to its original state, but with the inputs switched.

4.5 Summary

In this chapter, we have seen a demonstration of the negative coefficient of the thermal expansion in graphene by looking at the effect of heating graphene by way of the tunneling current. By taking $z(V)$ measurements at increasing tunneling current setpoints, we can transition from a smooth reversible measurement to a step-like measurement. This is explained in terms of the negative coefficient of thermal expansion in graphene. MD simulations are performed in order to demonstrate the effect of this thermal control. This shows that buckling can be induced through either an electrostatic or thermal load. This effect could potentially be used to create an electro-thermal actuation device.

Chapter 5

Graphene ripples modeled as a 2D Ising magnet

5.1 Ising Model

The Ising model was first proposed by Wilhelm Lenz as a thesis project for his student Ernst Ising in 1920. This simple, toy model had a chain of magnetic spins, which could be in either an up state or a down state, Lenz suspected that it might undergo a phase transition. The Hamiltonian for this model is given by

$$\mathcal{H} = -J \sum_{<i,j>} s_i s_j - H \sum_i s_i \tag{5.1}$$

where s_i is the ith spin, J is the spin-spin coupling constant and H is the external field.

The 1D Ising model was solved in Ising's 1924 thesis, but found that the 1D model underwent no phase transition. Ising then generalized this result, supposing that phase transitions were not possible in any number of dimensions.

This proved to be wrong. Rudolf Peierls demonstrated that the 2D Ising model does indeed undergo a phase transition, although he was unable to find the solution. It took Lars Onsager, in what is generally described as a mathematical tour de force to obtain the solution to the 2D Ising model in 1944[111]. Then, in the 1970s, Leo Kadanoff and Kenneth Wilson showed how to apply the renormalization group to the n-dimensional Ising model[112].

The Ising model occupies a special place in the realm of physics. It is one of the simplest models to undergo a phase transition. This makes it particularly well suited to studying the

concept of universality classes. Universality is the phenomena in which systems which at a microscopic level have nothing in common, display similar macroscopic behavior around the critical point. A universality class is characterized by a set exponents that govern behavior near the critical point.

It revealed that phase transitions were driven by fluctuations, and so revealed why mean field theories, which by definition consider the fluctuations to be of minimal importance, could never fully describe critical behavior near a phase transition[113].

Although relatively simple, the Ising model has proven to be powerful, and has found use in a number of disciplines[114–122]. It, of course, provided a mechanism for spontaneous magnetization. However the Ising model has also been used to describe island growth on GaAs [120]. A generalized Ising model, in which the coupling parameters J_{ij} can vary from spin to spin can be used to model behavior in neural networks[123, 124]. Its use has even been extended to the social sciences[125].

Due to the coupled, two state nature of ripples in graphene membranes, the Ising model is useful for describing the behavior of the ripples. Theoretical work by Bonilla and Carpio has looked at Ising spins coupled to the carbon atoms in a graphene membrane. These spins force the carbon atoms either up or down, resulting in the formation of a stable, rippled membrane[126–128]. Earlier studies have found some 2D membranes can undergo a wrinkling transition, and that this transition is similar to that of an Ising spin glass[129].

In this chapter we look at the behavior of suspended graphene membranes. We observe a transition for a flexible, reversible state to a rigid state. In the rigid state, it is possible to obtain atomic scale images of the graphene membrane. We model this transition using the celebrated 2D Ising model, and characterize the transition using four of the six critical Ising exponents.

5.2 Experimental Results

A series of $Z(V)$ curves taken with increasing setpoint currents are presented in Fig. 5.1(a). At a setpoint current of 0.1 nA, the tip bias is swept from 0-3.22 V, and the membrane is displaced a total distance of 46 nm. This is a reversible measurement. Increasing the setpoint current to 0.2 nA, results in an increase in the total displacement of the membrane during the measurement. This time, the total displacement is 55 nm. Further increase of the setpoint current to 0.5 nA results in a displacement of 57 nm. All three curves are reversible.

There is a fundamental change in the behavior of the $Z(V)$ curve as the setpoint current is increased to 1.0 nA. As the tip bias is ramped from 0.1-0.5 V, the height increases by 12 nm. At 0.5 V, there is a sudden 10 nm jump in the height of the membrane. As the tip bias continues to increase from 0.5 to 2.5 V, there is a slow increase in the height of the membrane from 25-30 nm. At 2.5 V, another jump occurs, resulting in a increase of height of another 25 nm, so that the final height of the membrane is 63 nm. Over the final stage of the tip bias ramp, from 2.5-3.22 V, there is little to no increase in the height of the membrane.

Increasing the setpoint current further, to 5.0 nA results in $Z(V)$ curves taken with very small increases in the height. These curves are reversible. Interestingly, even if the setpoint current is lowered below the critical setpoint, the $Z(V)$ curves still show very little movement.

The measured tunneling current is shown as a function of the tip bias in Fig. 5.1. This shows that the tunneling current is essentially held constant at the setpoint current value of 1.0 nA, except for spikes at 0.5 and 2.5 V. These current spikes mark points at which the membrane was moving too fast for the tip respond in time. However, both spikes are well below the saturation point of 50 nA, so we know that the tip did not crash, and the height of tip is faithfully tracking the movement of the membrane.

A topography map was acquired simultaneously with the critical $Z(V)$ curve. A line profile taken from the topography map is displayed in Fig. 5.1(c). This shows that after the critical $Z(V)$ measurement, there is a permanent increase in the height of the tip. The frozen
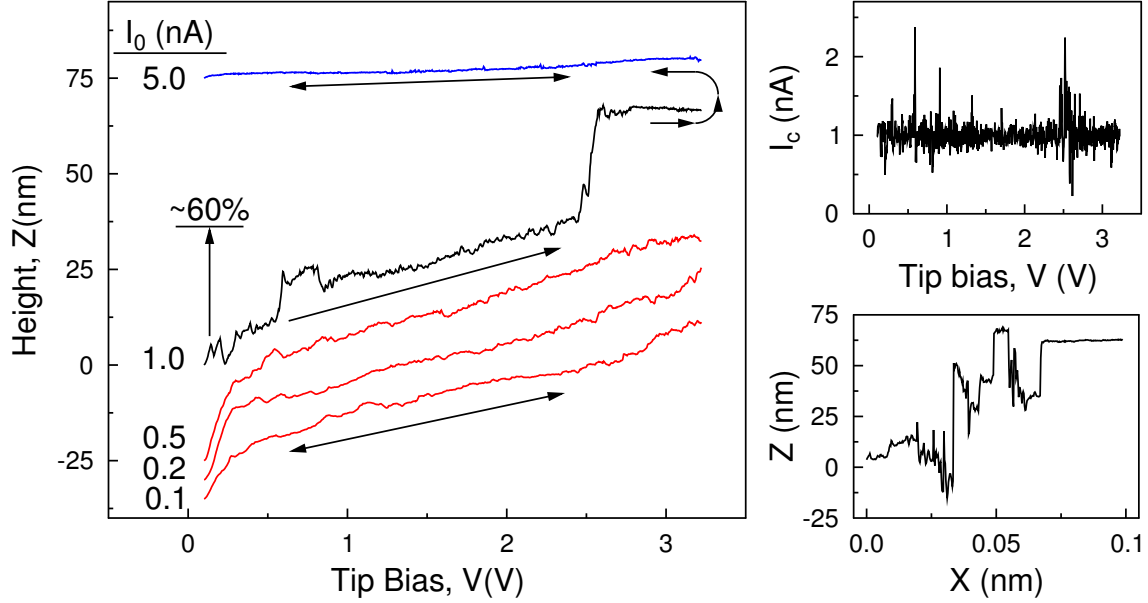
Figure 5.1: (a) A series of constant current $Z(V)$ curves taken at increasing setpoint current values. The red curves show the flexible, reversible state. The black curve shows the critical, irreversible state, and the blue curve shows the rigid, reversible state. These curves have been displayed with a slight offset for clarity (b) Tunneling current shown as a function of the tip bias for the critical $z(V)$ curve. (c) Line profile taken from a topography map acquired at the same time as the $z(V)$ curves. This line profile shows that the increase in tip height is permanent.

$Z(V)$ curves have been place above the critical curve to reflect this permanent increase in the height.

In the frozen state, it is possible to obtain images of graphene. A 6 nm × 6 nm image of graphene is shown in Figure 5.2(a). Here the honeycomb lattice can be resolved, and the image shows an overall curvature. The image can be characterized statistically by taking the site-site correlation as seen in Fig. 5.2(b). A line profile, taken diagonally across the image and displayed in Fig. 5.2(c). The line profile is peaked at the center, and then decays sharply, although it shows some small undulations due to the atomic corrugation. A log-log plot of the data is shown in Fig. 5.2(d). In the log-log plot, a line with a slope of 0.25 is shown for comparison
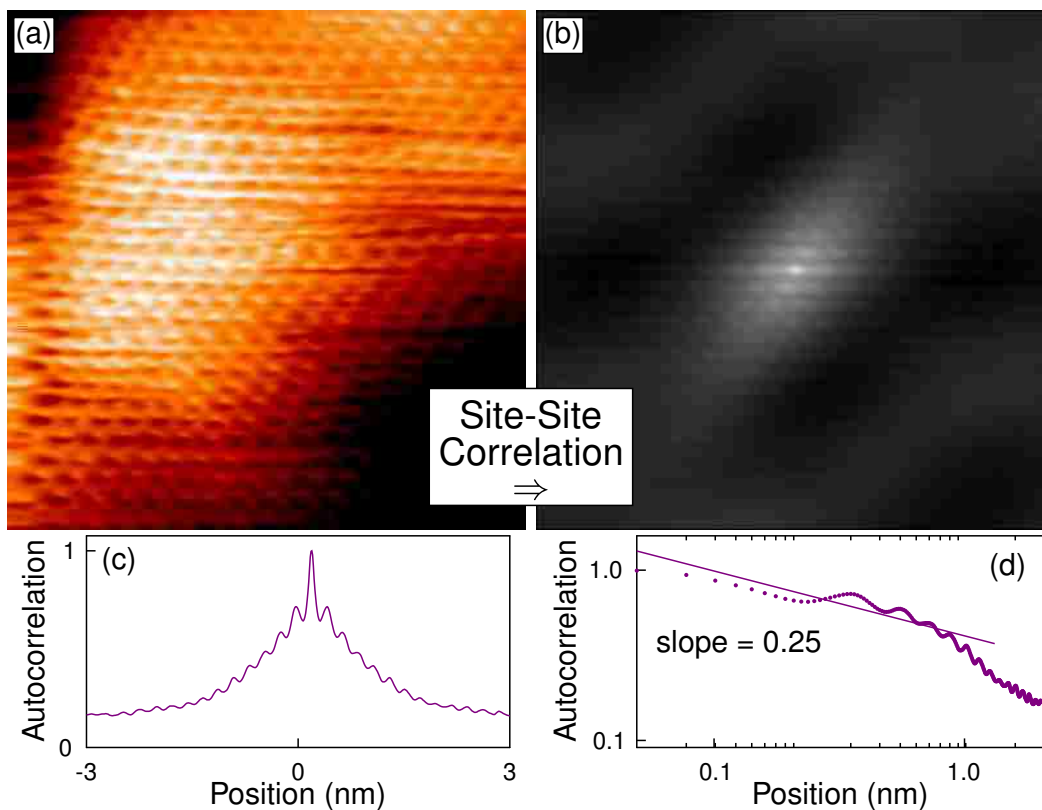
Figure 5.2: (a) Constant current, filled state STM image measuring 6 nm × 6 nm of a suspended graphene sample taken with a tip bias of 0.1 V and and setpoint tunneling current of 1.0 nA. (b) Site-site correlation function computed from the STM image in (a). (c) Line profile extracted from the site-site correlation function going from the bottom left corner, passing through the center of the image and ending in the top right. (d) Log Log plot of the positive half of the correlation function from (c). For comparison, a line with slope 1/4 is shown plotted with the line.

5.3 Theoretical Methods

To model the experimental results, the thermodynamic behavior of a modified 2D Ising magnet was simulated as a function of an external field having spatial dependence $h(r)$, and temperature T.

We can model the behavior of the graphene membrane using the Metropolis algorithm. The Metropolis algorithm is a well known single spin flip algorithm[130]. In this method, a lattice site is selected at random. The spin at the site is flipped, and the change in the energy between the two states is computed. If flipping the spin lowers the energy of the system, the change is accepted. If it raises the energy of the system, then the change is accepted according to the Boltzmann probability

$$p_i \propto \exp\left(\Delta E / kT\right) \tag{5.2}$$

The Hamiltonian used to calculate the energy of the system is given by

$$\mathcal{H} = -J(M) \sum_{<i,j>} s_i s_j - h(r) \sum_i s_i \tag{5.3}$$

where the individual Ising spins s_i represent the ripples of the graphene membrane, having either positive, or negative curvature. $J(M)$ is the coupling energy between spins, and is dependent upon the total magnetization

$$M = \sum_i s_i \tag{5.4}$$

The external field, $h(r) = h_0 e^{-r/\xi}$ is assumed to show an exponential decay with distance characterized by the correlation length ξ. We associate $J(M)$ with the elastic energy of the ripples. Local heating (due to the increasing tunneling current) contracts the graphene and increases $J(M)$ such that ripples are no longer favored. The last term in the Hamiltonian is related to the electrostatic energy between the tip and the sample and breaks the up-down

symmetry.

In the floppy state of graphene $J(M) = -1$ yields the desired antiferromagnetic coupling between nearest neighbor spins, while in the rigid state, $J(M) = 2$ is used to provide the desired ferromagnetic coupling. We performed Monte Carlo simulations using the Metropolis algorithm at different temperatures (in units of J/k_B on a hexagonal square lattice with 96000 sites but having an overall nearly square layout[130–132]. An individual spin s_i represents an entire ripple, having a diameter of 10 nm, which contains $\sim$1000 carbon atoms, giving us a scale transformation compared to Bonilla and Carpio[126, 128]

5.4   Numerical Results

Five characteristic magnetization-field $M(H)$ simulation curves are displayed in Fig. 5.3. All simulations were completed for strategic values of J, T and ξ (as labeled). The three lowest dashed curves (red) are characterized by a continuous, reversible increase in magnetization as the field increases. Notice that as the temperature is lowered, the overall magnetization increases slightly, as expected. Qualitatively, the three lower simulations are similar to the experimental $z(V)$ curves, with z playing the role of the order parameter, the bias voltage playing the role of the external field, and tunneling current playing the role of the temperature. However, as the tunneling current is increasing, the temperature in the Ising model simulation needs to be lowered in order to reproduce a similar trend. The next simulation result has a small jump followed by a larger permanent jump (as indicated by the one-way arrows). During the simulation run the first jump occurred because we increased the correlation length ξ from 8% to 11% (this length is compared to the inner radius of the simulation). The second jump occurs because the magnetization has reached 60-70% of its maximum, and at this point the overall nearest neighbor coupling, $J(M)$ is changed to be +2. This value, at the simulation temperature, makes the system ferromagnetic and below T_c. Therefore, even as the external field is lowered back to zero, the system stays ordered and follows the upper simulation dashed curve (blue) thereafter (as indicated by the
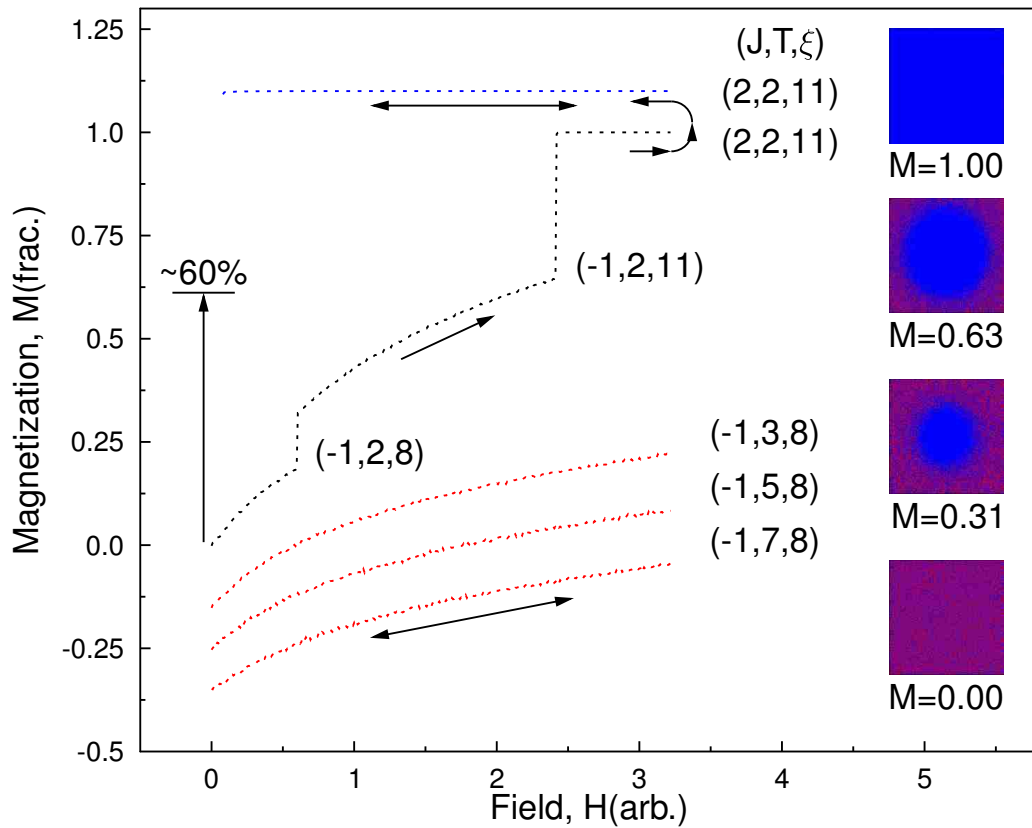
Figure 5.3: Dashed lines show the isothermal magnetization of a 2D Ising magnet for various values of J, T and ξ as labeled in the figure. These curves have been offset slightly for clarity. Along the righthand side, from top to bottom are real space images for different magnetization values as labeled.
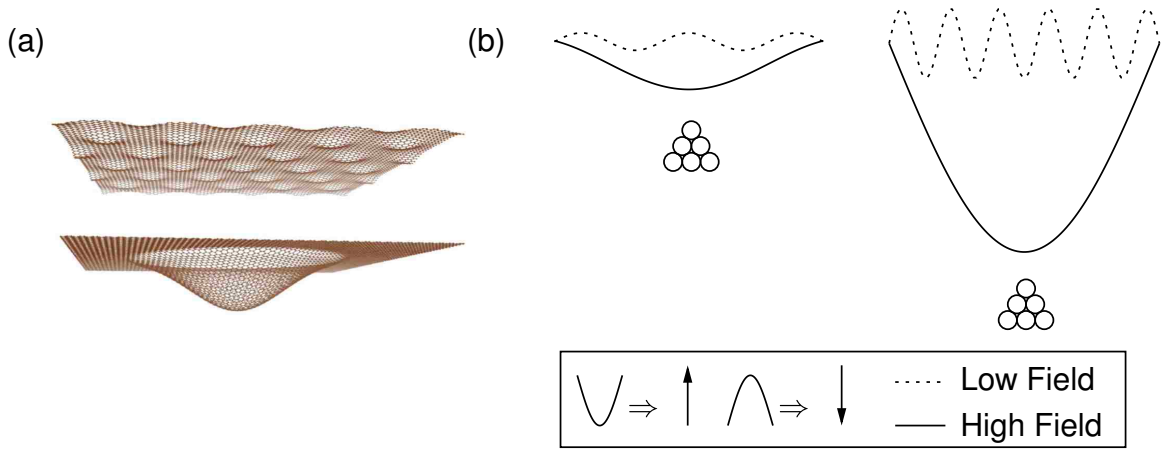
Figure 5.4: (a) Cartoon showing the graphene membrane in rigid state (top) and the rippled, flexible state (bottom). (b) Schematic showing the graphene membrane at low (left) and high (right) temperatures. The dashed line gives the shape of the graphene membrane for low tip bias values, and the solid line gives the shape at high tip bias values. Curved up (down) ripples represent spin up (down) elements.

arrows). The ordered simulations are very similar to the high current experimental $z(V)$ curves. Real-space images extracted from the simulations at four different magnetization values are shown as insets in Fig. 5.3(a).

5.5 Discussion

Experimentally, as we sweep through a wide range of voltages and then step through a large range of tunneling currents we are, in effect, hunting for the proper condition where the freestanding graphene will change from a floppy trampoline-type geometry as shown schematically in the upper model in Fig. 5.4(a) to a more rigid, larger, single curvature type structure shown in the lower model of Fig. 5.4(a). The reason the system changes its configuration is highlighted in a simple cross-sectional illustration with more details shown in Fig.5.4(b). At low current and low voltage, the graphene model is shown in Fig. 5.4(b). As the voltage is increased (shown by the solid curve on the left side), the ripples reverse their orientation and provide a mechanism for greater perpendicular displacement[133]. Next, as
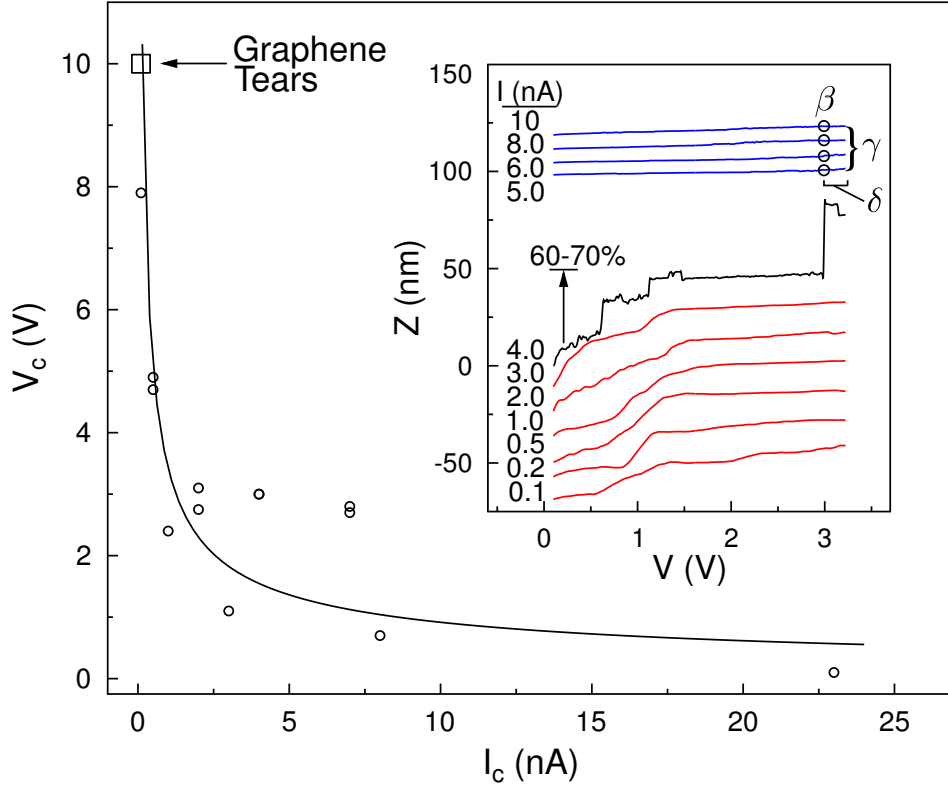
Figure 5.5: The critical potential plotted vs the critical tunneling current for several Ising-like transitions. (inset) One such set of data, along with labels for the critical exponents.

the current is increased, the graphene is heated and contracts, as depicted in the shorter wavelength illustration shown with the dashed curve in the right image of Fig. 5.4(b). The contraction leads to a larger elastic energy build up (like a compressed spring), making the system more unstable to perpendicular movement. This is similar to Euler buckling when a system is under uniaxial compression[134] (i.e., a vertical column buckling under too much weight). When more voltage is applied at the higher tunneling currents, the system suddenly jumps to form a larger structure which is both rigid and stable. This final state is the line in Fig. 5.4(b). Notice, that the role of temperature in our Ising model is two-fold. Temperature increases the entropy of the system as it normally would, but temperature also causes a contraction which increases the internal energy of the system and ultimately drives the change in geometry.

Quantity	2D Ising Ferromagnet	Freestanding Graphene Ripples	Measured Value	2D	3D
Pair Correlation Function ($T = T_c$)	$G(r) \sim r^{-\eta}$	$G(r) \sim r^{-\eta}$	$\eta = 0.27 \pm 0.03$	0.25	0.04
Critical Isotherm ($T = T_c$)	$M \sim H^{1/\delta}$	$|Z - Z_c| \sim |V - V_c|^{1/\delta}$	$\delta = 15 \pm 3$	15	5
Spontaneous Polarization	$M \sim |T - T_c|^{\beta}$	$|Z - Z_c| \sim |I^2 - I_c^2|^{\beta}$	$\beta = 0.12 \pm 0.03$	0.125	0.327
Susceptibility (χ)	$\partial M/\partial H \sim |T - T_c|^{-\gamma}$	$|\partial Z/\partial V| \sim |I^2 - I_c^2|^{-\gamma}$	$\gamma = 2.1 \pm 0.4$	1.25	1.23

Table 5.1: Measured critical exponents with predicted 2D and 3D values. V_c and I_c are the voltage at which the jump of height Z_c occurred for a particular dataset.

A large number of additional $z(V, I)$ data sets were acquired throughout the freestanding graphene surface and across numerous samples and the results are collected together in Fig. 5.5 All the current-voltage data pairs at which graphene transitions from flexible to rigid are shown as open circles. When the voltage range is reduced, we found that the sudden permanent jump to the rigid state still occurred, but at a much higher tunneling current setpoint; similarly when the voltage range was expanded, the jump then occurred at a much lower tunneling current setpoint. For the highest voltage range sweeps (0.01 to 10 V) graphene would sometimes tear, while for the lowest voltage range weeps the jump to the rigid state would sometimes not occur (note that most of the sweeps were in the normal range of up to 3 V so most of our data is for this condition). The overall result is consistent with $1/I^2$ behavior, in which thermal contraction at higher currents permits a lower voltage to drive the system into the rigid state. Remarkably, this trend also mimics the behavior of the critical field as a function of temperature for some ferromagnetic systems (i.e., H_c vs. T)[135]. Another, larger $z(V)$ data set showing the flexible state in red, a single jump $z(V)$ in black, and then several rigid $z(V)$ curves in blue. Notice, the jump occurs when the total height reaches 60-70% of the maximum.

The constant-current $z(V)$ data sets shown in Fig. 5.5 along with the STM image shown in Fig. 5.6 all provide strong evidence that this system follows the 2D Ising magnet Hamiltonian. However, quantifying a system's dimensionality and internal degrees of freedom requires the measurement of critical exponents. The large data set acquired as a function of current, voltage, and displacement made it possible to determine four of the six static 2D universal critical exponents, as listed in Table 5.1. Measuring just two of the critical exponents is enough to calculate the other six; so their interrelationships can be tested by measuring four. The pair correlation critical exponent η is a measure of the average domain size at the critical point. It was measured from the decay of the correlation function for several STM images similar to the one shown in Fig. 5.2, and our average value is in good agreement with the 2D Ising prediction. The critical isotherm exponent, δ characterizes the increase in

height with bias voltage along the critical isotherm (constant current). Its is calculated using the $z(V)$ data curve just after the sudden permanent increase in height and assumes that the electric field scales linearly with tip bias in the range of interest. Next, the spontaneous polarization critical exponent β describes the slow increase in height with temperature, in the ordered state and near the critical temperature. It is calculated using all the height current data sets acquired just after the sudden permanent jump for all the tip biases in the region of the jump, while assuming (from resistive heating arguments) that the local temperature increases with I^2 for the graphene beneath the STM tip[70]. Finally, the susceptibility critical exponent γ is a measure of how the susceptibility $\partial z/\partial V$ changes with temperature near the critical point. It is calculated for all the high-current data sets acquired just after the sudden permanent jump. This large set of critical exponents are all within the 2D Ising universality class[113], and therefore provide a rigorous testament of freestanding graphene's 2D Ising behavior.

One fascinating aspect for each fo these data sets is that the transition from the flexible state (above T_c) to the rigid state (below T_c occurs with increasing current, that is , when heating up the sample, which is opposite to the usual 2D Ising magnet behavior. This is a consequence of graphene's unusual negative thermal expansion coefficient[86, 108, 136–138]. Graphene contracts rather than expands when heated. Thus, when graphene is heated and the internal tension increases, this changes the coupling between the nearest-neighbor ripples. In effect it alters the lowest energy configuration for graphene from the antiferromagetic state to the bulged out ferromagnetic state.

5.6   Summary

In summary, this study successfully applied the 2D magnetic Ising model to the technologically-important freestanding graphene system. Four universal 2D critical exponents were measured, twice the number required, using constant-current STM displacement measurements in concert with atomic-resolution STM surface images. Unexpectedly, a transition was ob-

served between a flexible state and a rigid state as the sample was heated (opposite the 2D Ising system); this is explained in terms of the negative thermal expansion properties of graphene. We presented a model in which individual graphene ripples are the spins of a 2D magnet, with the distinction that the elastic energy of the ripples increase during heating due to thermal contraction. What we observe is that once the elastic energy increases above a certain level the freestanding graphene ripple geometry transforms from antiferromagenetic ordering to ferromagnetic ordering.
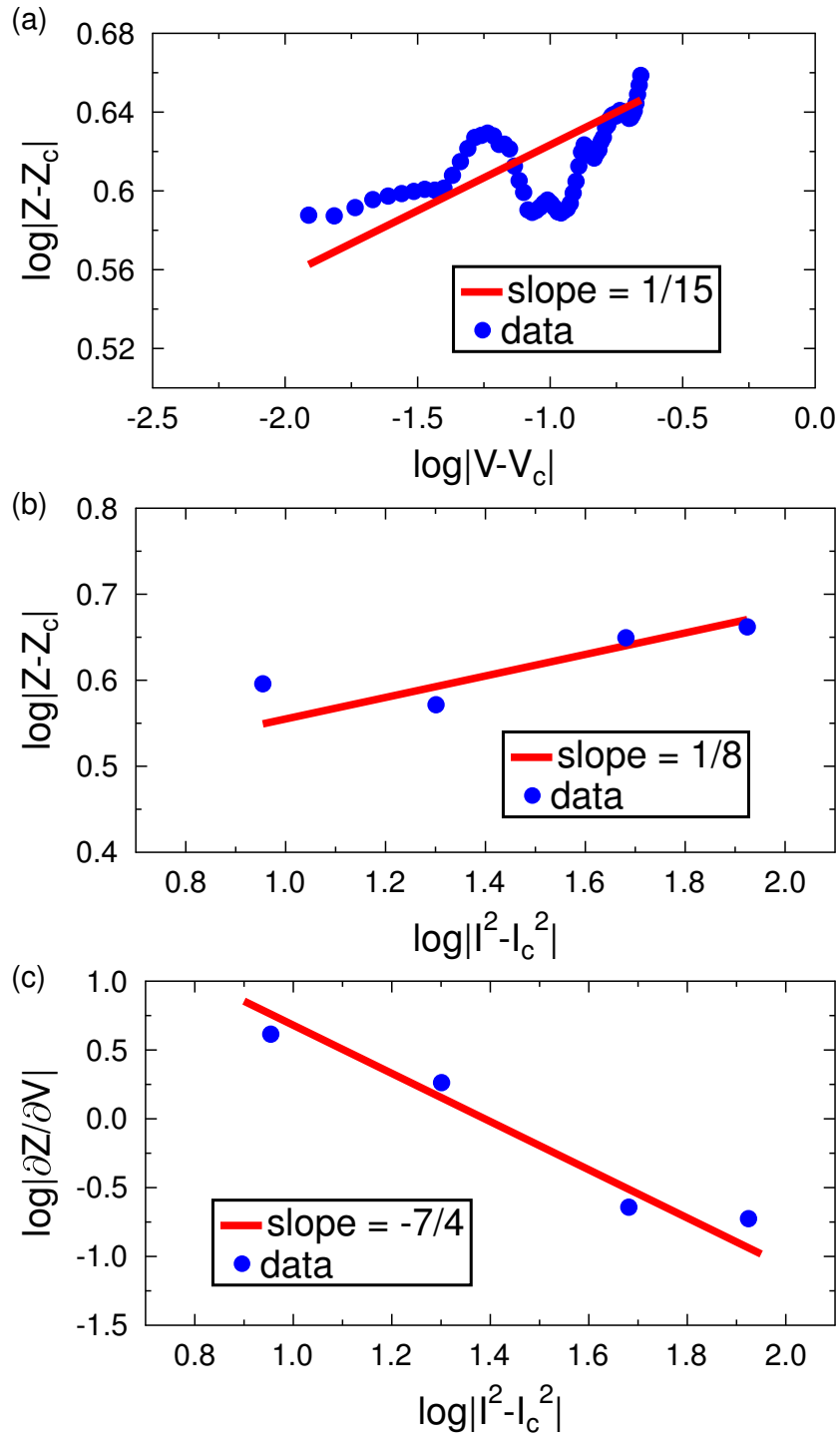
Figure 5.6: (a) Plot showing the data used to calculate the critical exponent δ (b) Plot showing the data used to calculate the critical exponent β (c) Plot showing the data used to calculate the critical exponent γ

Chapter 6

Conclusion

Graphene is a material that shows great technical promise. It has amazing electronic properties, and also shows potential for mechanical applications. Suspended graphene is particularly useful as its properties are unaffected by external strains or charge puddling that is observed in graphene samples supported by various substrates. In this dissertation I have shown how to manipulate graphene on a nanometer scale using scanning tunneling microscopy.

First, the I demonstrate the effects of the tip bias on a suspended graphene membrane. Bringing a biased STM tip to within a short distance of a suspended graphene sample leads to an electrostatic attraction between the tip and the sample. When using the STM tip to image suspended graphene membranes, this attractive force leads to an enhanced atomic corrugation up 20 times larger than the expected value. This size of this corrugation shows a dependence upon the scan speed of the STM tip. This indicates that the suspended graphene is moving under the influence of the STM tip. In addition, by sweeping the tip bias over a predetermined range we can generate a large electrostatic attraction between the tip and the sample. By sweeping the tip bias while maintaining a constant setpoint current, and monitoring the resulting changes in the height of the STM tip, it is possible to observe reversible displacements of the graphene membrane between 20-70 nm. This physical movement of the graphene sample under the influence of the STM tip can lead to changes in the electronic structure of graphene.

Next, I explore the effects of the setpoint current on the behavior of the graphene mem-

brane. Increasing the setpoint current leads to local heating of the graphene sample. Since graphene has a negative coefficient of thermal expansion, as it is heated, it pulls away from the STM tip. This shows that using STM we gan generate a thermal load. The sign of the thermal load depends upon the geometry of the graphene sample. If the thermal load is aligned with the electrostatic load from the STM tip, large buckling events can be generated. These buckling events mark the transition of the graphene sample from a dynamic, flexible configuration to a rigid, static one

Finally these buckling transitions are described using the language of the 2D Ising model. The ripples, with either positive or negative curvature can be described as individual Ising spins. Using Monte Carlo simulations, the buckling transition is modeled as an antiferromagnetic to ferromagnetic transition. In addition, due to the wealth of $z(V, I)$ data collected with the STM, this transition can be characterized using four of the six static critical exponents of the 2D Ising model. This measurement place the graphene in the Ising universality class.

This work shows the promise of graphene in the context of electrothermal mechanical devices. This buckling transition could form the basis of a graphene based electrothermal mechanical actuator.

Bibliography

[1] K. S. Novoselov. Electric field effect in atomically thin carbon films. *Science*, 306(5696):666669, Oct 2004.

[2] K. S. Novoselov, A. K. Geim, S. V. Morozov, D. Jiang, M. I. Katsnelson, I. V. Grigorieva, S. V. Dubonos, and A. A. Firsov. Two-dimensional gas of massless dirac fermions in graphene. *Nature*, 438(7065):197200, Nov 2005.

[3] K. S. Novoselov, D. Jiang, F. Schedin, T. J. Booth, V. V. Khotkevich, S. V. Morozov, and A. K. Geim. Two-dimensional atomic crystals. *Proceedings of the National Academy of Sciences*, 102(30):1045110453, Jul 2005.

[4] A. K. Geim and K. S. Novoselov. The rise of graphene. *Nature Materials*, 6(3):183191, Mar 2007.

[5] A. H. Castro Neto, N. M. R. Peres, K. S. Novoselov, and A. K. Geim. The electronic properties of graphene. *Rev. Mod. Phys.*, 81(1):109162, Jan 2009.

[6] K. I. Bolotin, K. J. Sikes, J. Hone, H. L. Stormer, and P. Kim. Temperature-dependent transport in suspended graphene. *Physical Review Letters*, 101(9), Aug 2008.

[7] K.I. Bolotin, K.J. Sikes, Z. Jiang, M. Klima, G. Fudenberg, J. Hone, P. Kim, and H.L. Stormer. Ultrahigh electron mobility in suspended graphene. *Solid State Communications*, 146(9-10):351355, Jun 2008.

[8] S. Morozov, K. Novoselov, M. Katsnelson, F. Schedin, D. Elias, J. Jaszczak, and A. Geim. Giant intrinsic carrier mobilities in graphene and its bilayer. *Physical Review Letters*, 100(1), Jan 2008.

[9] Xu Du, Ivan Skachko, Anthony Barker, and Eva Y. Andrei. Approaching ballistic transport in suspended graphene. *Nature Nanotechnology*, 3(8):491495, Jul 2008.

[10] Jens Baringhaus, Ming Ruan, Frederik Edler, Antonio Tejeda, Muriel Sicot, Amina Taleb-Ibrahimi, An-Ping Li, Zhigang Jiang, Edward H. Conrad, Claire Berger, and et al. Exceptional ballistic transport in epitaxial graphene nanoribbons. *Nature*, 506(7488):349354, Feb 2014.

[11] Alexander A. Balandin, Suchismita Ghosh, Wenzhong Bao, Irene Calizo, Desalegne Teweldebrhan, Feng Miao, and Chun Ning Lau. Superior thermal conductivity of single-layer graphene. *Nano Lett.*, 8(3):902907, Mar 2008.

[12] L. Dong, J. Hansen, P. Xu, M. L. Ackerman, S. D. Barber, J. K. Schoelz, D. Qi, and P. M. Thibado. Electromechanical properties of freestanding graphene functionalized with tin oxide (sno2) nanoparticles. *Appl. Phys. Lett.*, 101(6):061601, 2012.

[13] S. Hu, M. Lozada-Hidalgo, F. C. Wang, A. Mishchenko, F. Schedin, R. R. Nair, E. W. Hill, D. W. Boukhvalov, M. I. Katsnelson, R. A. W. Dryfe, and et al. Proton transport through one-atom-thick crystals. *Nature*, 516(7530):227230, Nov 2014.

[14] P. Xu, M. Neek-Amal, S. D. Barber, J. K. Schoelz, M. L. Ackerman, P. M. Thibado, A. Sadeghi, and F. M. Peeters. Unusual ultra-low-frequency fluctuations in freestanding graphene. *Nature Communications*, 5, Apr 2014.

[15] Sungjin Park, Jinho An, Ji Won Suk, and Rodney S. Ruoff. Graphene-based actuators. *Small*, 6(2):210212, Jan 2010.

[16] J. S. Bunch, A. M. van der Zande, S. S. Verbridge, I. W. Frank, D. M. Tanenbaum, J. M. Parpia, H. G. Craighead, and P. L. McEuen. Electromechanical resonators from graphene sheets. *Science*, 315(5811):490493, Jan 2007.

[17] Arend M. van der Zande, Robert A. Barton, Jonathan S. Alden, Carlos S. Ruiz-Vargas, William S. Whitney, Phi H. Q. Pham, Jiwoong Park, Jeevak M. Parpia, Harold G. Craighead, and Paul L. McEuen. Large-scale arrays of single-layer graphene resonators. *Nano Lett.*, 10(12):48694873, Dec 2010.

[18] C. Lee, X. Wei, J. W. Kysar, and J. Hone. Measurement of the elastic properties and intrinsic strength of monolayer graphene. *Science*, 321(5887):385388, Jul 2008.

[19] P. Wallace. The band theory of graphite. *Phys. Rev.*, 71(9):622634, May 1947.

[20] Gordon Semenoff. Condensed-matter simulation of a three-dimensional anomaly. *Physical Review Letters*, 53(26):24492452, Dec 1984.

[21] Paul McEuen, Marc Bockrath, David Cobden, Young-Gui Yoon, and Steven Louie. Disorder, pseudospins, and backscattering in carbon nanotubes. *Physical Review Letters*, 83(24):50985101, Dec 1999.

[22] Yuanbo Zhang, Yan-Wen Tan, Horst L. Stormer, and Philip Kim. Experimental observation of the quantum hall effect and berrys phase in graphene. *Nature*, 438(7065):201204, Nov 2005.

[23] R. R. Nair, P. Blake, A. N. Grigorenko, K. S. Novoselov, T. J. Booth, T. Stauber, N. M. R. Peres, and A. K. Geim. Fine structure constant defines visual transparency of graphene. *Science*, 320(5881):13081308, Jun 2008.

[24] F. Guinea, M. I. Katsnelson, and A. K. Geim. Energy gaps and a zero-field quantum hall effect in graphene by strain engineering. *Nat Phys*, 6(1):3033, Sep 2009.

[25] N. Levy, S. A. Burke, K. L. Meaker, M. Panlasigui, A. Zettl, F. Guinea, A. H. C. Neto, and M. F. Crommie. Strain-induced pseudo-magnetic fields greater than 300 Tesla in

graphene nanobubbles. *Science*, 329(5991):544547, Jul 2010.

[26] Claire Berger, Zhimin Song, Tianbo Li, Xuebin Li, Asmerom Y. Ogbazghi, Rui Feng, Zhenting Dai, Alexei N. Marchenkov, Edward H. Conrad, Phillip N. First, and et al. Ultrathin epitaxial graphite: 2D electron gas properties and a route toward graphene-based nanoelectronics. *The Journal of Physical Chemistry B*, 108(52):1991219916, Dec 2004.

[27] B. K. Daas, Sabih U. Omar, S. Shetu, Kevin M. Daniels, S. Ma, T. S. Sudarshan, and M. V. S. Chandrashekhar. Comparison of epitaxial graphene growth on polar and nonpolar 6H-SiC faces: On the growth of multilayer films. *Crystal Growth & Design*, 12(7):33793387, Jul 2012.

[28] K. V. Emtsev, F. Speck, Th. Seyller, and L. Ley. Interaction, growth, and ordering of epitaxial graphene on SiC0001 surfaces: A comparative photoelectron spectroscopy study. *Phys. Rev. B*, 77(15), Apr 2008.

[29] Peng Xu, Matthew L. Ackerman, Steven D. Barber, James K. Schoelz, Dejun Qi, Paul M. Thibado, Virginia D. Wheeler, Luke O. Nyakiti, Rachael L. Myers-Ward, and Charles R. Eddy Jr. Graphene manipulation on 4H-SiC(0001) using scanning tunneling microscopy. *Jpn. J. Appl. Phys.*, 52(3R):035104, Mar 2013.

[30] Peng Xu, Steven D. Barber, J. Kevin Schoelz, Matthew L. Ackerman, Dejun Qi, Paul M. Thibado, Virginia D. Wheeler, Luke O. Nyakiti, Rachael L. Myers-Ward, and Charles R. Eddy. Atomic-scale movement induced in nanoridges by scanning tunneling microscopy on epitaxial graphene grown on 4H-SiC(0001). *J. Vac. Sci. Technol. B*, 31(4):04D101, 2013.

[31] P. Xu, D. Qi, J.K. Schoelz, J. Thompson, P.M. Thibado, V.D. Wheeler, L.O. Nyakiti, R.L. Myers-Ward, C.R. Eddy, D.K. Gaskill, and et al. Multilayer graphene, moir patterns, grain boundaries and defects identified by scanning tunneling microscopy on the m-plane, non-polar surface of SiC. *Carbon*, 80:7581, Dec 2014.

[32] Alfonso Reina, Xiaoting Jia, John Ho, Daniel Nezich, Hyungbin Son, Vladimir Bulovic, Mildred S. Dresselhaus, and Jing Kong. Large area, few-layer graphene films on arbitrary substrates by chemical vapor deposition. *Nano Lett.*, 9(1):3035, Jan 2009.

[33] Sukang Bae, Hyeongkeun Kim, Youngbin Lee, Xiangfan Xu, Jae-Sung Park, Yi Zheng, Jayakumar Balakrishnan, Tian Lei, Hye Ri Kim, Young Il Song, and et al. Roll-to-roll production of 30-inch graphene films for transparent electrodes. *Nature Nanotechnology*, 5(8):574578, Jun 2010.

[34] Yuanbo Zhang, Victor W. Brar, Caglar Girit, Alex Zettl, and Michael F. Crommie. Origin of spatial charge inhomogeneity in graphene. *Nat Phys*, 5(10):722726, Aug 2009.

[35] A. Pirkle, J. Chan, A. Venugopal, D. Hinojos, C. W. Magnuson, S. McDonnell, L. Colombo, E. M. Vogel, R. S. Ruoff, and R. M. Wallace. The effect of chemical residues on the physical and electrical properties of chemical vapor deposited graphene

transferred to sio2. *Appl. Phys. Lett.*, 99(12):122108, 2011.

[36] N. D. Mermin and H. Wagner. Absence of ferromagnetism or antiferromagnetism in one- or two-dimensional isotropic heisenberg models. *Physical Review Letters*, 17(22):11331136, Nov 1966.

[37] N. Mermin. Crystalline order in two dimensions. *Phys. Rev.*, 176(1):250254, Dec 1968.

[38] Martin Zinke-Allmang, Leonard C. Feldman, and Marcia H. Grabow. Clustering on surfaces. *Surface Science Reports*, 16(8):377463, Dec 1992.

[39] J A Venables, G D T Spiller, and M Hanbucken. Nucleation and growth of thin films. *Reports on Progress in Physics*, 47(4):399459, Apr 1984.

[40] A. Fasolino, J. H. Los, and M. I. Katsnelson. Intrinsic ripples in graphene. *Nature Materials*, 6(11):858861, Sep 2007.

[41] D.R. Nelson and L. Peliti. Fluctuations in membranes with crystalline and hexatic order. *J. Phys. France*, 48(7):10851092, 1987.

[42] Leo Radzihovsky and David Nelson. Statistical mechanics of randomly polymerized membranes. *Phys. Rev. A*, 44(6):35253542, Sep 1991.

[43] D.R. Nelson, Piran T., and S. Weiberg, editors. *Statistical mechanics of membranes and surfaces*. World Scientific, Singapore, 2004.

[44] P. L. de Andres, F. Guinea, and M. I. Katsnelson. Bending modes, anharmonic effects, and thermal expansion coefficient in single-layer and multilayer graphene. *Phys. Rev. B*, 86(14), Oct 2012.

[45] L. Lindsay, D. A. Broido, and Natalio Mingo. Flexural phonons and thermal transport in graphene. *Phys. Rev. B*, 82(11), Sep 2010.

[46] Jannik C. Meyer, A. K. Geim, M. I. Katsnelson, K. S. Novoselov, T. J. Booth, and S. Roth. The structure of suspended graphene sheets. *Nature*, 446(7131):6063, Mar 2007.

[47] P. Xu, Yurong Yang, S. D. Barber, M. L. Ackerman, J. K. Schoelz, D. Qi, Igor A. Kornev, Lifeng Dong, L. Bellaiche, Salvador Barraza-Lopez, and et al. Atomic control of strain in freestanding graphene. *Phys. Rev. B*, 85(12), Mar 2012.

[48] Recep Zan, Chris Muryn, Ursel Bangert, Philip Mattocks, Paul Wincott, David Vaughan, Xuesong Li, Luigi Colombo, Rodney S. Ruoff, Bruce Hamilton, and et al. Scanning tunnelling microscopy of suspended graphene. *Nanoscale*, 4(10):3065, 2012.

[49] N. N. Klimov, S. Jung, S. Zhu, T. Li, C. A. Wright, S. D. Solares, D. B. Newell, N. B. Zhitenev, and J. A. Stroscio. Electromechanical properties of graphene drumheads. *Science*, 336(6088):15571561, Jun 2012.

[50] Peng Xu, Lifeng Dong, Mehdi Neek-Amal, Matthew L. Ackerman, Jianhua Yu, Steven D. Barber, James Kevin Schoelz, Dejun Qi, Fangfang Xu, Paul M. Thibado, and et al. Self-organized platinum nanoparticles on freestanding graphene. *ACS Nano*, 8(3):26972703, Mar 2014.

[51] J.K. Schoelz, P. Xu, S.D. Barber, D. Qi, M.L. Ackerman, G. Basnet, C.T. Cook, and P.M. Thibado. High-percentage success method for preparing and pre-evaluating tungsten tips for atomic-resolution scanning tunneling microscopy. *J. Vac. Sci. Technol. B*, 30(3):033201, 2012.

[52] P. Xu, J. K. Schoelz, S. D. Barber, M. L. Ackerman, and P. M. Thibado. Broad frequency and amplitude control of vibration in freestanding graphene via scanning tunneling microscopy with calculated dynamic pseudo-magnetic fields. *Journal of Applied Physics*, 112(12):124317, 2012.

[53] M. Neek-Amal, P. Xu, J.K. Schoelz, M.L. Ackerman, S.D. Barber, P.M. Thibado, A. Sadeghi, and F.M. Peeters. Thermal mirror buckling in freestanding graphene locally controlled by scanning tunnelling microscopy. *Nature Communications*, 5:4962, Sep 2014.

[54] J. K. Schoelz, P. Xu, V. Meunier, P. Kumar, M. Neek-Amal, P. M. Thibado, and F. M. Peeters. Graphene ripples as a realization of a two-dimensional ising model: A scanning tunneling microscope study. *Phys. Rev. B*, 91(4), Jan 2015.

[55] E. W. Muller. Field ion microscopy. *Science*, 149(3684):591601, Aug 1965.

[56] G. Binnig, H. Rohrer, Ch. Gerber, and E. Weibel. Surface studies by scanning tunneling microscopy. *Physical Review Letters*, 49(1):5761, Jul 1982.

[57] G. Binnig, H. Rohrer, C. Gerber, and E. Weibel. Tunneling through a controllable vacuum gap. *Appl. Phys. Lett.*, 40(2):178, 1982.

[58] G. Binnig, H. Rohrer, Ch. Gerber, and E. Weibel. 7 x 7 reconstruction on Si(111) resolved in real space. *Physical Review Letters*, 50(2):120123, Jan 1983.

[59] Joseph Stroscio, R. Feenstra, and A. Fein. Electronic structure of the si(111)2 1 Surface by scanning-tunneling microscopy. *Physical Review Letters*, 57(20):25792582, Nov 1986.

[60] R. Feenstra, Joseph Stroscio, J. Tersoff, and A. Fein. Atom-selective imaging of the GaAs(110) surface. *Physical Review Letters*, 58(12):11921195, Mar 1987.

[61] V. LaBella, H. Yang, D. Bullock, P. Thibado, Peter Kratzer, and Matthias Scheffler. Atomic structure of the GaAs(001)-(24) surface resolved using scanning tunneling microscopy and first-principles theory. *Physical Review Letters*, 83(15):29892992, Oct 1999.

[62] Y. Mo, J. Kleiner, M. Webb, and M. Lagally. Activation energy for surface diffusion

of Si on Si(001): A scanning-tunneling-microscopy study. *Physical Review Letters*, 66(15):19982001, Apr 1991.

[63] H Yang, V.P LaBella, D.W Bullock, Z Ding, J.B Smathers, and P.M Thibado. Activation energy for Ga diffusion on the GaAs(001)-(2 x 4) surface: an MBE-STM study. *Journal of Crystal Growth*, 201-202:8892, May 1999.

[64] B. Swartzentruber. Direct measurement of surface diffusion using atom-tracking scanning tunneling microscopy. *Physical Review Letters*, 76(3):459462, Jan 1996.

[65] D. M. Eigler and E. K. Schweizer. Positioning single atoms with a scanning tunnelling microscope. *Nature*, 344(6266):524526, Apr 1990.

[66] M. F. Crommie, C. P. Lutz, and D. M. Eigler. Confinement of electrons to quantum corrals on a metal surface. *Science*, 262(5131):218220, Oct 1993.

[67] M. F. Crommie, C. P. Lutz, and D. M. Eigler. Imaging standing waves in a two-dimensional electron gas. *Nature*, 363(6429):524527, Jun 1993.

[68] J. A. Stroscio, J. and D. M. Eigler. Atomic and molecular manipulation with the scanning tunneling microscope. *Science*, 254(5036):13191326, Nov 1991.

[69] U. Staufer. Tailoring nanostructures with a scanning tunneling microscope. *J. Vac. Sci. Technol. B*, 9(2):1389, Mar 1991.

[70] Roland Wiesendanger. *Scanning Probe Microscopy and Spectroscopy: Methods and Applications*. Cambridge University Press, 1994.

[71] Richard Liboff. *Introductory Quantum Mechanics*. Addison-Wesley, 2002.

[72] J. Bardeen. Tunnelling from a many-particle point of view. *Physical Review Letters*, 6(2):5759, Jan 1961.

[73] J. Tersoff and D. R. Hamann. Theory and application for the scanning tunneling microscope. *Physical Review Letters*, 50(25):19982001, Jun 1983.

[74] Alex Pronschinske, Daniel J. Mardit, and Daniel B. Dougherty. Modeling the constant-current distance-voltage mode of scanning tunneling spectroscopy. *Phys. Rev. B*, 84(20), Nov 2011.

[75] Ilona Sitnitsky, John J. Garramone, Joseph Abel, Peng Xu, Steven D. Barber, Matt L. Ackerman, J. Kevin Schoelz, Paul M. Thibado, and Vincent P. LaBella. Schottky barrier and attenuation length for hot hole injection in nonepitaxial au on p-type GaAs. *J. Vac. Sci. Technol. B*, 30(4):04E110, 2012.

[76] H. Mizes, Sang-il Park, and W. Harrison. Multiple-tip interpretation of anomalous scanning-tunneling-microscopy images of layered materials. *Phys. Rev. B*, 36(8):44914494, Sep 1987.

[77] Allan J. Melmed. The art and science and other aspects of making sharp tips. *J. Vac. Sci. Technol. B*, 9(2):601, Mar 1991.

[78] J. P. Ibe. On the electrochemical etching of tips for scanning tunneling microscopy. *J. Vac. Sci. Technol. A*, 8(4):3570, Jul 1990.

[79] M. Kulawik, M. Nowicki, G. Thielsch, L. Cramer, H.-P. Rust, H.-J. Freund, T. P. Pearl, and P. S. Weiss. A double lamellae dropoff etching procedure for tungsten tips attached to tuning fork atomic force microscopy/scanning tunneling microscopy sensors. *Review of Scientific Instruments*, 74(2):1027, 2003.

[80] Mircea Fotino. Tip sharpening by normal and reverse electrochemical etching. *Review of Scientific Instruments*, 64(1):159, 1993.

[81] F. Bastiman, A. G. Cullis, M. Hopkinson, and K. J. Briston. Two step optimized process for scanning tunneling microscopy tip fabrication. *J. Vac. Sci. Technol. B*, 28(2):371, 2010.

[82] Bing-Feng Ju, Yuan-Liu Chen, and Yaozheng Ge. The art of electrochemical etching for preparing tungsten probes with controllable tip profile and characteristic parameters. *Review of Scientific Instruments*, 82(1):013707, 2011.

[83] M. Klein and G. Schwitzgebel. An improved lamellae drop-off technique for sharp tip preparation in scanning tunneling microscopy. *Review of Scientific Instruments*, 68(8):3099, 1997.

[84] Gobind Basnet, James Kevin Schoelz, Peng Xu, Steven D. Barber, Matthew L. Ackerman, and Paul M. Thibado. Etch-stop method for reliably fabricating sharp yet mechanically stable scanning tunneling microscope tips. *J. Vac. Sci. Technol. B*, 31(4):043201, 2013.

[85] C. L. Kane and E. J. Mele. Size, shape, and low energy electronic structure of carbon nanotubes. *Physical Review Letters*, 78(10):19321935, Mar 1997.

[86] Wenzhong Bao, Feng Miao, Zhen Chen, Hang Zhang, Wanyoung Jang, Chris Dames, and Chun Ning Lau. Controlled ripple texturing of suspended graphene and ultrathin graphite membranes. *Nature Nanotechnology*, 4(9):562566, Jul 2009.

[87] Franz R. Eder, Jani Kotakoski, Katharina Holzweber, Clemens Mangler, Viera Skakalova, and Jannik C. Meyer. Probing from both sides: Reshaping the graphene landscape via face-to-face dual-probe microscopy. *Nano Lett.*, 13(5):19341940, May 2013.

[88] Graphene supermarket: https://graphene-supermarket.com/.

[89] Lisa A. Hockett and Stephen E. Creager. A convenient method for removing surface oxides from tungsten stm tips. *Review of Scientific Instruments*, 64(1):263, 1993.

[90] P. Xu, Y. Yang, S. D. Barber, M. L. Ackerman, J. K. Schoelz, Igor A. Kornev, Sal-

vador Barraza-Lopez, L. Bellaiche, and P. M. Thibado. Giant surface charge density of graphene resolved from scanning tunneling microscopy and first-principles theory. *Phys. Rev. B*, 84(16), Oct 2011.

[91] Peng Xu, Steven D. Barber, Matthew L. Ackerman, James Kevin Schoelz, and Paul M. Thibado. Role of bias voltage and tunneling current in the perpendicular displacements of freestanding graphene via scanning tunneling microscopy. *J. Vac. Sci. Technol. B*, 31(4):04D103, 2013.

[92] Bogdana Borca, Sara Barja, Manuela Garnica, Marina Minniti, Antonio Politano, Josefa M Rodriguez-Garca, Juan Jose Hinarejos, Daniel Faras, Amadeo L Vzquez de Parga, and Rodolfo Miranda. Electronic and geometric corrugation of periodically rippled, self-nanostructured graphene epitaxially grown on ru(0001). *New Journal of Physics*, 12(9):093018, Sep 2010.

[93] E. N. Voloshina, E. Fertitta, A. Garhofer, F. Mittendorfer, M. Fonin, A. Thissen, and Yu. S. Dedkov. Electronic structure and imaging contrast of graphene moire on metals. *Sci. Rep.*, 3, Jan 2013.

[94] Fernando F. Dall'Agnol and Victor P. Mammana. Solution for the electric potential distribution produced by sphere-plane electrodes using the method of images. *Rev. Bras. Ensino Fs.*, 31(3):3503.13503.9, 2009.

[95] C. Julian Chen. Theory of scanning tunneling spectroscopy. *J. Vac. Sci. Technol. A*, 6(2):319, Mar 1988.

[96] W H Duan and C M Wang. Nonlinear bending and stretching of a circular graphene sheet under a central point load. *Nanotechnology*, 20(7):075702, Jan 2009.

[97] Hidekatsu Suzuura and Tsuneya Ando. Phonons and electron-phonon scattering in carbon nanotubes. *Phys. Rev. B*, 65(23), May 2002.

[98] A. Morpurgo and F. Guinea. Intervalley scattering, long-range disorder, and effective time-reversal symmetry breaking in graphene. *Physical Review Letters*, 97(19), Nov 2006.

[99] Chun-Chung Chen, Wenzhong Bao, Jesse Theiss, Chris Dames, Chun Ning Lau, and Stephen B. Cronin. Raman spectroscopy of ripple formation in suspended graphene. *Nano Lett.*, 9(12):41724176, Dec 2009.

[100] T. Mashoff, M. Pratzer, V. Geringer, T. J. Echtermeyer, M. C. Lemme, M. Liebmann, and M. Morgenstern. Bistability and oscillatory motion of natural nanomembranes appearing within monolayer graphene on silicon dioxide. *Nano Lett.*, 10(2):461465, Feb 2010.

[101] Niklas Lindahl, Daniel Midtvedt, Johannes Svensson, Oleg A. Nerushev, Niclas Lindvall, Andreas Isacsson, and Eleanor E. B. Campbell. Determination of the bending rigidity of graphene via electrostatic actuation of buckled membranes. *Nano Lett.*,

12(7):35263531, Jul 2012.

[102] Timothy Moulton and G.K Ananthasuresh. Micromechanical devices with embedded electro-thermal-compliant actuation. *Sensors and Actuators A: Physical*, 90(1-2):3848, May 2001.

[103] Yuanbo Zhang, Victor W. Brar, Feng Wang, Caglar Girit, Yossi Yayon, Melissa Panlasigui, Alex Zettl, and Michael F. Crommie. Giant phonon-induced conductance in scanning tunnelling spectroscopy of gate-tunable graphene. *Nat Phys*, 4(8):627630, Jul 2008.

[104] Thomas Frederiksen, Mads Brandbyge, Nicols Lorente, and Antti-Pekka Jauho. Inelastic scattering and local heating in atomic gold wires. *Physical Review Letters*, 93(25), Dec 2004.

[105] Thomas Frederiksen, Magnus Paulsson, Mads Brandbyge, and Antti-Pekka Jauho. Inelastic transport theory from first principles: Methodology and application to nanoscale devices. *Phys. Rev. B*, 75(20), May 2007.

[106] Duhee Yoon, Young-Woo Son, and Hyeonsik Cheong. Negative thermal expansion coefficient of graphene measured by raman spectroscopy. *Nano Lett.*, 11(8):32273231, Aug 2011.

[107] F. Flores, P. Echenique, and R. Ritchie. Energy dissipation processes in scanning tunneling microscopy. *Phys. Rev. B*, 34(4):28992902, Aug 1986.

[108] G. Savarino. A general physics laboratory investigation of the thermodynamics of a rubber band. *Am. J. Phys.*, 59(2):141, 1991.

[109] M. Neek-Amal and F. M. Peeters. Lattice thermal properties of graphane: Thermal contraction, roughness, and heat capacity. *Phys. Rev. B*, 83(23), Jun 2011.

[110] Ali Sadeghi, Alexis Baratoff, S. Alireza Ghasemi, Stefan Goedecker, Thilo Glatzel, Shigeki Kawai, and Ernst Meyer. Multiscale approach for simulations of kelvin probe force microscopy with atomic resolution. *Phys. Rev. B*, 86(7), Aug 2012.

[111] Lars Onsager. Crystal statistics. i. a two-dimensional model with an order-disorder transition. *Phys. Rev.*, 65(3-4):117149, Feb 1944.

[112] Kenneth Wilson. The renormalization group: Critical phenomena and the kondo problem. *Rev. Mod. Phys.*, 47(4):773840, Oct 1975.

[113] R K Pathria. *Statistical Mechanics, Third Edition*. Academic Press, 2011.

[114] T. Lee and C. Yang. Statistical theory of equations of state and phase transitions. ii. lattice gas and ising model. *Phys. Rev.*, 87(3):410419, Aug 1952.

[115] Zvi Friedman. Critical exponents for the three-dimensional ising model from the real-space renormalization group in two dimensions. *Physical Review Letters*,

36(22):13261328, May 1976.

[116] R. Hocken and M. Moldover. Ising critical exponents in real fluids: An experiment. *Physical Review Letters*, 37(1):2932, Jul 1976.

[117] S. Janssen, D. Schwahn, and T. Springer. Mean-field ising crossover and the critical exponents , , and for a polymer blend: d-pb/ps studied by small-angle neutron scattering. *Physical Review Letters*, 68(21):31803183, May 1992.

[118] LEO KADANOFF, WOLFGANG Gotze, DAVID HAMBLEN, ROBERT HECHT, E. LEWIS, V. PALCIAUSKAS, MARTIN RAYL, J. SWIFT, DAVID ASPNES, and JOSEPH KANE. Static phenomena near critical points: Theory and experiment. *Rev. Mod. Phys.*, 39(2):395431, Apr 1967.

[119] Pradeep Kumar, Giancarlo Franzese, and H. Stanley. Predictions of dynamic behavior under pressure for two scenarios to explain water anomalies. *Physical Review Letters*, 100(10), Mar 2008.

[120] V. LaBella, D. Bullock, M. Anser, Z. Ding, C. Emery, L. Bellaiche, and P. Thibado. Microscopic view of a two-dimensional lattice-gas ising system within the grand canonical ensemble. *Physical Review Letters*, 84(18):41524155, May 2000.

[121] Z. Ding, D. Bullock, P. Thibado, V. LaBella, and Kieran Mullen. Atomic-scale observation of temperature and pressure driven preroughening and roughening. *Physical Review Letters*, 90(21), May 2003.

[122] Z Ding, D.W Bullock, P.M Thibado, V.P LaBella, and Kieran Mullen. Time-evolution of the GaAs(001) pre-roughening process. *Surface Science*, 540(2-3):491496, Aug 2003.

[123] Daniel Fraiman, Pablo Balenzuela, Jennifer Foss, and Dante Chialvo. Ising-like dynamics in large-scale functional brain networks. *Phys. Rev. E*, 79(6), Jun 2009.

[124] Yasser Roudi, Joanna Tyrcha, and John Hertz. Ising model for neural data: Model quality and approximate methods for extracting functional connectivity. *Phys. Rev. E*, 79(5), May 2009.

[125] K Suchecki, V. M Eguluz, and M. San Miguel. Conservation laws for the voter model in complex networks. *Europhysics Letters (EPL)*, 69(2):228234, Jan 2005.

[126] L L Bonilla and A Carpio. Ripples in a graphene membrane coupled to glauber spins. *Journal of Statistical Mechanics: Theory and Experiment*, 2012(09):P09015, Sep 2012.

[127] L. L. Bonilla, A. Carpio, A. Prados, and R. R. Rosales. Ripples in a string coupled to glauber spins. *Phys. Rev. E*, 85(3), Mar 2012.

[128] L. L. Bonilla and A. Carpio. Model of ripples in graphene. *Phys. Rev. B*, 86(19), Nov 2012.

[129] Carlo Carraro and David Nelson. Grain-boundary buckling and spin-glass models of

disorder in membranes. *Phys. Rev. E*, 48(4):30823090, Oct 1993.

[130] Nicholas Metropolis, Arianna W. Rosenbluth, Marshall N. Rosenbluth, Augusta H. Teller, and Edward Teller. Equation of state calculations by fast computing machines. *The Journal of Chemical Physics*, 21(6):1087, 1953.

[131] W. K. Hastings. Monte Carlo sampling methods using Markov chains and their applications. *Biometrika*, 57(1):97109, 1970.

[132] V. P. LaBella, D. W. Bullock, Z. Ding, C. Emery, W. G. Harter, and P. M. Thibado. Monte Carlo derived diffusion parameters for ga on the GaAs(001)- (24) surface: A molecular beam epitaxyscanning tunneling microscopy study. *J. Vac. Sci. Technol. A*, 18(4):1526, 2000.

[133] A. Taskin, A. Lavrov, and Yoichi Ando. Ising-like spin anisotropy and competing antiferromagnetic-ferromagnetic orders in gdbaco2o5.5 Single crystals. *Physical Review Letters*, 90(22), Jun 2003.

[134] Jin Wu Jiang. The buckling of single-layer mos 2 under uniaxial compression. *Nanotechnology*, 25(35):355402, Aug 2014.

[135] Carolin Antoniak, Markus E. Gruner, Marina Spasova, Anastasia V. Trunova, Florian M. Rmer, Anne Warland, Bernhard Krumme, Kai Fauth, Shouheng Sun, Peter Entel, and et al. A guideline for atomistic design and understanding of ultrahard nanomagnets. *Nature Communications*, 2:528, Nov 2011.

[136] K. Zakharchenko, M. Katsnelson, and A. Fasolino. Finite temperature lattice properties of graphene beyond the quasiharmonic approximation. *Physical Review Letters*, 102(4), Jan 2009.

[137] Monica Pozzo, Dario Alf, Paolo Lacovig, Philip Hofmann, Silvano Lizzit, and Alessandro Baraldi. Thermal expansion of supported and freestanding graphene: Lattice constant versus interatomic distance. *Physical Review Letters*, 106(13), Mar 2011.

[138] Nicolas Mounet and Nicola Marzari. First-principles determination of the structural, vibrational and thermodynamic properties of diamond, graphite, and derivatives. *Phys. Rev. B*, 71(20), May 2005.

Appendix A

List of Publications and Presentations

A.1   Refereed Journal Publications

1. **J.K. Schoelz**, P. Xu, V. Meunier, P. Kumar, M. Neek-Amal, P.M. Thibado, and F.M. Peeters. Graphene ripples as a realization of a 2D Ising model: a scanning tunneling microscopy. *Phys. Rev. B* **91** 045413 (2015)

2. M. Neek-Amal, P. Xu, **J.K. Schoelz**, M.L. Ackerman, S.D. Barber, P.M. Thibado, A. Sadeghi, and F.M. Peeters. Thermal mirror buckling in freestanding graphene locally controlled by scanning tunneling microscopy. *Nat. Comm.* **5** 4962 (2014)

3. P. Xu, D. Qi, **J.K. Schoelz**, J. Thompson, P.M. Thibado, V.D. Wheeler, L.O. Nyakiti. R.L. Myers Ward, C.R. Eddy D.K. Gaskill, M. Neek Amal, F.M. Peeters. Multilayer graphene, Moiré patterns, grain boundaries and defects identified by scanning tunneling microscopy on the m-plane, non-polar surface of SiC. *Carbon* (2014)

4. P. Xu, M. Neek-Amal, S.D. Barber, M.L. Ackerman, **J.K. Schoelz**, P.M. Thibado, A. Sadeghi, and F.M. Peeters. Unusual ultra-low frequency fluctuations in freestanding graphene. *Nat. Comm.* **5** 3720 (2014)

5. P. Xu, L. Dong, M. Neek-Amal, M.L. Ackerman, J. Yu, S.D. Barber, **J.K. Schoelz**, D. Qi, F. Xu, P.M. Thibado and F.M. Peeters. Self organized platinum nanoparticles on freestanding graphene. *ACS Nano* (2014)

6. P. Xu, M.L. Ackerman, S.D. Barber, **J.K. Schoelz**, P.M. Thibado, V.D. Wheeler, L.O. Nyakiti, R.L. Myers-Ward, C.R. Eddy, Jr, and D.K. Gaskill. Competing scanning tunneling microscope tip-interlayer interactions for twisted multilayer graphene on the a-plane SiC surface. *Surface Science* **617**, 113-117 (2013)

7. G. Basnet, **J.K. Schoelz**, P. Xu, S.D. Barber, M.L. Ackerman, P.M. Thibado. Etch stop method for reliably fabricating sharp yet mechanically stable scanning tunneling microscope tips. *J. Vac. Sci. Tech. B* **31**(4), 043201 (2013)

8. P. Xu, S.D. Barber, M.L. Ackerman, **J.K. Schoelz**, P.M. Thibado. Role of bias voltage and tunneling current in the perpendicular displacements of freestanding graphene via scanning tunneling microscopy. *J. Vac. Sci. Tech. B* **31**(4), 04D103 (2013)

9. P. Xu, S.D. Barber, **J.K. Schoelz**, M.L. Ackerman, D. Qi, P.M. Thibado, V.D. Wheeler, L.O. Nyakiti, R.L. Myers-Ward, C.R. Eddy Jr., and D.K. Gaskill. Atomic-scale movement induced in nanoridges by scanning tunneling microscopy on epitaxial graphene grown on 4H-SiC(0001). *J. Vac. Sci. Tech. B* **31**(4), 04D101 (2013)

10. P. Xu, M.L. Ackerman, S.D. Barber, **J.K. Schoelz**, D. Qi, P.M. Thibado, V.D. Wheeler, L.O. Nyakiti, R.L. Myers-Ward, C.R. Eddy Jr., and D.K. Gaskill. Graphene manipulation on 4H-SiC(0001) using scanning tunneling microscopy. *Japanese Journal of Applied Physics* **52** 035104 (2013)

11. P. Xu, **J.K. Schoelz**, S.D. Barber, M.L. Ackerman, and P.M. Thibado. Broad frequency and amplitude control of vibration in freestanding graphene via scanning tunneling microscopy with calculated dynamic pseudo-magnetic fields. *J. Appl. Phys.* **112**, 124317 (2012).

12. P. Xu, Y. Yang, D. Qi, S.D. Barber, **J.K. Schoelz**, M.L. Ackerman, L. Bellaiche, and P.M. Thibado. Electronic transition from graphite to graphene via controlled movement of the top layer with scanning tunneling microscopy. *Phys. Rev. B* **86**, 085428 (2012) *[Selected by the editors of PRB to be an Editors' Suggestion]*

13. L. Dong, J. Hanson, P. Xu, M.L. Ackerman, S.D. Barber, **J.K. Schoelz**, D. Qi, and P.M. Thibado. Electromechanical properties of freestanding graphene functionalized with tin oxide (SnO_2) nanoparticles. *Appl. Phys. Lett.* **101**, 061601 (2012)

14. I. Sitnitsky, J.J. Garramone, J. Abel, P. Xu, S.D. Barber, M.L. Ackerman, **J.K. Schoelz**, P.M. Thibado, V.P. Labella. Schottky barrier and attenuation length for hot hole injection in non-epitaxial Au on p type GaAs. *J. Vac. Sci Tech B* **30**(4), 04E110 (2012)

15. P. Xu, Y. Yang, S.D. Barber, **J.K. Schoelz**, D. Qi, M.L. Ackerman, L. Bellaiche, P.M. Thibado. Tunable Electronic Reconstruction from graphite to graphene. *Carbon* **50**, 4633 (2012)

16. P. Xu, Y. Yang, D. Qi, S.D. Barber, M.L. Ackerman, **J.K. Schoelz**, T.B. Bothwell, S. Barraza-Lopez, L. Bellaiche, and P.M. Thibado. A pathway between ABA- and ABC-stacked graphene layers with scanning tunneling micrscopy. *Appl. Phys. Lett.* **100**, 201601(2012)

17. **J.K. Schoelz**, P. Xu, S.D. Barber, D. Qi, M.L. Ackerman, G. Basnet, C.T. Cook and P.M. Thibado. High-Percentage Success Method for Preparing and Pre-Evaluating Tungsten Tips for Atomic-Resolution Scanning Tunneling Microscopy. *J. Vac. Sci. Tech B* **30** 3(2012) [Winner of the 2012 AVS Vacuum Technology Division's Shop Note Award]

18. P. Xu, Y. Yang, S.D. Barber, M.L. Ackerman, **J.K. Schoelz**, D. Qi, I.A. Kornev, L. Dong, L. Bellaiche, S. Barraza-Lopez and P.M. Thibado. Atomic control of strain in freestanding graphene. *Phys. Rev. B.* **85**, 12406(2012)

19. P. Xu, Y. Yang, S.D. Barber, M.L. Ackerman, **J.K. Schoelz**, I.A. Kornev, S. Barraza-Lopez, L. Bellaiche, P.M. Thibado. Giant surface charge density of graphene resolved from scanning tunneling microscopy and first-principles theory. *Phys. Rev. B.* **84** 161409(2011)

20. W. Li, J.D. Gunton, S.J. Khan, **J.K. Schoelz**, and A. Chakrabarti. Brownian dynamics simulation of insulin microsphere formation form break-up of a fractal network. *J. Chem. Phys.* **134**, 024902 (2011)

A.2 Posters

1. **J.K. Schoelz**, M. Neek-Amal, M.L. Ackerman, P. Xu, S.D. Barber, P. Kumar, V. Meunier, A. Sadeghi, P.M. Thibado and F.M. Peeters. Thermal mirror buckling in freestanding graphene films induced by a scanning tunneling microscope tip *University of Arkansas INBRE conference 2014*

2. **J.K. Schoelz**, P. Xu, M.L. Ackerman and P.M. Thibado. Large displacements in graphene films induced by changes in the tunneling parameters *University of Arkansas INBRE conference 2013*

3. **J.K. Schoelz**, P. Xu, Y. Yang, S.D. Barber, D. Qi, M.L. Ackerman L. Bellaiche, P.M. Thibado. Scanning Tunneling Microscopy used to Facilitate the Graphite to Graphene Transition through Vertical Translation of the Top Layer *University of Arkansas INBRE conference 2012*

4. P. Xu, Y. Yang, S.D. Barber, **J.K. Schoelz**, D. Qi, M.L. Ackerman, L. Bellaiche, P.M. Thibado. Tunable Electronic Reconstruction from graphite to graphene *Physical Electronics Conference 2012*

5. P. Xu, **J.K. Schoelz**, G. Basnet, C. Cook, S.D Barber, M.L Ackerman, D. Qi, and P.M. Thibado. Evaluating a double lamella technique for etching tungsten wire STM tips using cone angle *University of Arkansas INBRE conference 2011*

6. P. Xu, **J.K. Schoelz**, G. Basnet, C. Cook, S.D. Barber, M.L. Ackerman, D. Qi, and P.M. Thibado. Evaluating Automated STM Tip Making Procedures Using Quantitative Optical Photographs and Graphite *Physical Electronics Conference 2011*

A.3 Conference Talks

1. **J.K. Schoelz**, P. Xu, M. Neek-Amal, S.D. Barber, M.L. Ackerman, P.M. Thibado, A. Sadeghi, and F.M. Peeters. Unusual ultralow frequency fluctuations in freestanding graphene membranes *Physical Electronics Conference 2014*

2. **J.K. Schoelz**, M. Neek-Amal, P. Xu, S.D. Barber, M.L. Ackerman, A. Sadeghi, P.M. Thibado and F.M. Peeters. Mirror buckling in freestanding graphene membranes induced by a scanning tunneling microscope tip *APS March Meeting 2014*

3. **J.K. Schoelz**, P. Xu, S.D. Barber, M.L. Ackerman and P.M. Thibado. Current and voltage dependent interactions between a scanning tunneling microscopy tip and a freestanding graphene sample *APS March Meeting 2013*

Appendix B

Code for 2D Ising Model

Here is the FORTRAN90 code for the Monte Carlo simulations carried out in Chapter 5

```
!
! Start by defining constants that will be used all over the code
!



!J:           defined below
!r00:         Size of the STM tip
!potmin:      min value of potential
!potmax:      max value of potential
!temperature: Temperature of the simulation
!dim1,dim2:   Define the size of the lattice
!maxiter:     number of Monte Carlo step per subcalculation
!npot:        number of potential values,
!nkt:         number of temperature values
!spin:        this is where we store the spin

module constants
real(kind=8) :: J
```

```fortran
real(kind=8), parameter :: r00=37.0D0

real(kind=8), parameter :: potmin=0.1D0

real(kind=8), parameter :: potmax=200.0D0

real(kind=8), parameter :: temperature=2.0D0

integer, parameter :: dim1=240, dim2=400

integer, parameter :: maxiter=5000000

integer :: npot= 400, nkt=4


integer, dimension(dim1*dim2) :: spin

logical, parameter :: afm=.true.

logical, parameter :: cold=.false.

end module constants




!

! Subroutine to define a hexagonal lattice

!


subroutine lattice(d1,d2,r)

implicit none

!4 atoms per cell

integer, intent(in) :: d1, d2

real(kind=8), dimension(d1*d2,2), intent(inout) :: r

real(kind=8), dimension(4,2) :: r0

real(kind=8), dimension(2) :: lattice1, lattice2

integer :: dim1, dim2
```

```fortran
integer :: i, j, k

dim1=d1/2
dim2=d2/2
r0(1,:)=(/0.0D0,sqrt(3.0D0)/2.0D0/)
r0(2,:)=(/0.5D0,0.0D0/)
r0(3,:)=(/1.5D0,0.0D0/)
r0(4,:)=(/2.0D0,sqrt(3.0D0)/2.0D0/)
lattice1=(/3.0d0,0.0D0/)
lattice2=(/0.0D0,sqrt(3.0D0)/)
k=0
!row
do i=1,dim1
do j=1,4
k=k+1
r(k,:)=r0(j,:)+(i-1)*lattice1
end do
end do

!column
do i=2,dim2
do j=1,4*dim1
k=k+1
r(k,:)=r(j,:)+(i-1)*lattice2
end do
end do
```

```fortran
! Save grid of positions

!open(unit=1,file="honey.xyz")

!write(1,*) 4*dim1*dim2

!write(1,*)

!do i=1,4*dim1*dim2

! write(1,*) " C", r(i,:), 0.0

!end do

!close(unit=1)

end subroutine lattice




!

! Main Program

!


program ising2d

use constants

implicit none

integer  k, ii, jj, ipot, ikt, l


! ----- variables for portable seed setting -----

INTEGER :: i_seed

INTEGER, DIMENSION(:), ALLOCATABLE :: a_seed

INTEGER, DIMENSION(1:8) :: dt_seed

! ----- end of variables for seed setting -----
```

```
real(kind=8) :: r, eold, pot, deltae, e0, dpot,r3(3)

real(kind=8) :: rr(dim1*dim2),pot0

real(kind=8) :: kt, p

real(kind=8) :: magnetization, temp

real(kind=8), dimension(:), allocatable :: potential

real(kind=8), dimension(:,:), allocatable :: r0

real(kind=8), dimension(:), allocatable :: val1

real(kind=8), dimension(:), allocatable :: val2

INTEGER, DIMENSION(:), ALLOCATABLE :: nvo

INTEGER, DIMENSION(:,:), ALLOCATABLE :: ind

character(len=64) :: filename




! Save some memory for

! r0--Atomic Positions

! nvo--Adjacency Matrix

allocate(r0(dim1*dim2,2))

allocate(nvo(dim1*dim2))

nvo=0

allocate(ind(dim1*dim2,3))




! Call the lattice subroutine in order to define the hexagonal

lattice positions call lattice(dim1,dim2,r0)
```

```fortran
! Center the atoms in order to place the tip at (0,0)
do ii=1,2
r0(:,ii)=r0(:,ii)-sum(r0(:,ii))/dim1/dim2
end do




! Set the size of the interaction between the STM tip and various spins
allocate(val1(dim1*dim2))
do ii=1,dim1*dim2
val1(ii)=exp(-(sqrt(r0(ii,1)**2+r0(ii,2)**2))/(0.75*r00))
end do


allocate(val2(dim1*dim2))
do ii=1,dim1*dim2
val2(ii)=exp(-(sqrt(r0(ii,1)**2+r0(ii,2)**2))/(r00))
end do




! Compute the adjacency matrix. We will use
! periodic boundary conditions
do ii=1,dim1*dim2
```

```fortran
do jj=ii+1,dim1*dim2

do k=-1,1

do l=-1,1

if(sqrt((r0(ii,1)-r0(jj,1)+k*3.0D0*dim1/2.0)**2

+(r0(ii,2)-r0(jj,2)+l*dim2*sqrt(3.0D0)/2.0D0)**2)<1.2) then

nvo(ii)=nvo(ii)+1

nvo(jj)=nvo(jj)+1

if(nvo(ii)>3 .or. nvo(jj)>3) stop "too many neighbors"

ind(ii,nvo(ii))=jj

ind(jj,nvo(jj))=ii

end if

end do

end do

end do

if(nvo(ii)/=3) write(*,*) ii, nvo(ii)

end do




! Use the current time, in order to generate

! random seed for lattice

CALL RANDOM_SEED(size=i_seed)

ALLOCATE(a_seed(1:i_seed))

CALL RANDOM_SEED(get=a_seed)

CALL DATE_AND_TIME(values=dt_seed)

a_seed(i_seed)=dt_seed(8); a_seed(1)=dt_seed(8)*dt_seed(7)*dt_seed(6)

CALL RANDOM_SEED(put=a_seed)
```

```fortran
DEALLOCATE(a_seed)

! ! ----- Done setting up random seed -----



! Set up the sweep over the potential (tip bias)
dpot=(potmax-potmin)/(npot-1.0D0) ! Define potential spacing
allocate(potential(2*npot)) ! Save memory for potential values
potential(1)=0.0 ! Potential starts at zero
potential(2*npot)=0.0 ! Potential ends at zero
do ipot=2,npot ! Potential runs from potmin to potmax
potential(ipot)=potential(ipot-1)+dpot
potential(2*npot-ipot)=potential(ipot)
end do


!initial magnetization
magnetization=0.0D0
!do ikt=1,nkt !loop over temperatures (i.e. injected current)
kt=temperature
do ipot=1,npot !loop over potential from tip
pot=potential(ipot)
if((ipot==1.or.cold).and..not.afm) then
call random_number(rr)
write(*,*) "First step", ipot==1, cold, "temperature=",kt
do ii=1,dim1*dim2
spin(ii)=1
if(rr(ii)<=0.5) spin(ii)=-1
end do
```

```fortran
!at the beginning of each sweep, we redine
!the grid at AFM (i.e, presumably the
!ground state in graphene)
else if(ipot==1.and.afm) then
write(*,*) "First step AFM ", "temperature=",kt
spin=0
spin(1)=1.0
do while(sum(abs(spin))<dim1*dim2)
do ii=1,dim1*dim2
if(spin(ii)==0) cycle
do jj=1,nvo(ii)
spin(ind(ii,jj))=-spin(ii)
end do
end do
end do
end if




!loop over Monte-Carlo
loopi:do k=1,maxiter
!note that in this version of the code, we do not use r3(2)
call random_number(r3)
!Randomly select a position
ii=int(r3(1)*dim1*dim2)+1
```

```fortran
! Find the tip effect on this atom
if(pot<37.25) then
pot0=pot*val1(ii)
else
pot0=pot*val2(ii)
end if




! Define the lattice to be antiferromagnetic
if(pot<150) then
J= -1
else
J=2
end if




!Run the Metropolis algorithm to decide
!whether or not to flip the spin
call spin_flip(ii,r3(3),kt,J,pot0,ind)
end do loopi




magnetization=0.0D0
do ii=1,dim1*dim2
magnetization=magnetization+spin(ii)
end do
magnetization=magnetization/(dim1*dim2)
```

```fortran
write(1,*) kt, dpot*(ipot-1), magnetization, pot

end do

write(filename,'(i3)') ikt

filename="spin.dat"//adjustl(filename)

call plotspin(r0,spin,dim1*dim2,trim(filename))

write(*,*) "Final Magnetization=", magnetization, "at temperature:", kt

write(1,*)

!end do

end program ising2d




subroutine plotspin(r,spin,nat,filename)

implicit none

real(kind=8), dimension(nat,2), intent(in) :: r

integer, dimension(nat), intent(in) :: spin

integer, intent(in) :: nat

character(*), intent(in) :: filename

integer :: i




open(unit=2,file=trim(filename))

do i=1,nat

write(2,*) r(i,:), spin(i)

end do

close(unit=2)

end subroutine plotspin
```

```fortran
!
! Subroutine: This is where we apply the Metropolis algoithm
! to decide whether or not to flip a spin
!


subroutine spin_flip(i,r,kt,JJ,pot,ind)
! From the constants module, we grab the spin lattice
  use constants, only : spin, dim1, dim2
! as well as the dimensions of the lattice
implicit none
! Sets spin lattice position
integer, intent(in) :: i
integer, dimension(dim1*dim2,3), intent(in) :: ind
! Set potential, distance from tip, spin-spin coupling constant
real(kind=8), intent(in) :: pot, r, JJ, kt
! Temperature
real(kind=8) :: temp, DeltaE, proba



temp=-JJ*(spin(ind(i,1))+spin(ind(i,2))+spin(ind(i,3)))
! Find the difference in Energy between the two states
DeltaE=-2.0D0*(temp*spin(i)-pot*spin(i))
! Flip the spin
spin(i)=-spin(i)
```

```
if(DeltaE<0.0D0) return

! If change in Energy is negative, then we might flip it back

proba=dexp(-DeltaE/kt)

if(proba>r) return

spin(i)=-spin(i)

return

end subroutine spin_flip
```